JOINT INSTITUTE FOR AERONAUTICS AND ACOUSTICS

National Aeronautics and
Space Administration

Ames Research Center

JIAA TR - 96

Stanford University

A CFD Study of Tilt Rotor Flowfields

By

Ian Fejtek and Leonard Roberts

Stanford University
Department of Aeronautics and Astronautics
Stanford, CA 94305

October 1989

Abstract

The download on the wing produced by the rotor wake of a tilt rotor vehicle in hover is of major concern because of its severe impact on payload-carrying capability. In a concerted effort to understand the fundamental fluid dynamics that causes this download, and to help find ways to reduce it, computational fluid dynamics is employed to study this problem. The thin-layer Navier-Stokes equations are used to describe the flow, and an implicit, finite difference numerical algorithm is the method of solution. This report is a summary of the methodology developed to analyze the tilt rotor flowfield. Included are discussions of computations of an airfoil and wing in freestream flows at -90 degrees, a rotor alone, and wing/rotor interaction in two and three dimensions. Preliminary results demonstrate the feasibility and great potential of the present approach. Recommendations are made for both near-term and far-term improvements to the method.

Contents

List of Figures

List of Symbols

a	speed of sound
A	rotor disk area, or flux Jacobian matrix in the ξ-direction
b	wing span
B	flux Jacobian matrix in the η-direction
c	wing chord
c_p	specific heat at constant pressure
C	flux Jacobian matrix in the ζ-direction
C_p	pressure coefficient
D_ξ, D_η, D_ζ	diagonal matrices associated with the LU-ADI algorithm
e	total energy per unit volume
e_i	internal energy per unit mass
E	inviscid flux vector in the ξ-direction
F	inviscid flux vector in the η-direction
G	inviscid flux vector in the ζ-direction
G_v	viscous flux vector in the ζ-direction
I	identity matrix
J	transformation Jacobian
k	coefficient of thermal conductivity
L_ξ, L_η, L_ζ	lower bidiagonal matrices associated with the LU-ADI algorithm
M	viscous flux Jacobian matrix in the ζ-direction
M_∞	freestream Mach number
p	pressure
Pr	Prandtl number
Q	vector of conserved quantities

r	radial location
R	rotor radius
Re	Reynolds number
t	time
T_ξ, T_η, T_ζ	similarity transformation matrices
u, v, w	Cartesian velocity components
U_ξ, U_η, U_ζ	upper bidiagonal matrices associated with the LU-ADI algorithm
U, V, W	contravariant velocity components
x, y, z	Cartesian coordinates

α	angle of incidence
γ	ratio of specific heats
$\delta_\xi, \delta_\eta, \delta_\zeta$	central difference operators
$\Delta_\xi, \Delta_\eta, \Delta_\zeta$	forward difference operators
$\nabla_\xi, \nabla_\eta, \nabla_\zeta$	backward difference operators
ϵ	artificial dissipation coefficient
ξ, η, ζ	chordwise, spanwise, and normal coordinates in body conforming system
Λ_ξ	diagonal matrix of eigenvalues associated with the flux Jacobian matrix A
Λ_η	diagonal matrix of eigenvalues associated with the flux Jacobian matrix B
Λ_ζ	diagonal matrix of eigenvalues associated with the flux Jacobian matrix C
μ	coefficient of viscosity
ρ	density
ω	angular frequency of rotation

Chapter 1

Introduction

1.1 Motivation

The tilt rotor aircraft is a flight vehicle which combines the vertical takeoff and landing capability of the helicopter with the efficient high-speed cruise performance of conventional fixed-wing aircraft. The tilt rotor vehicle has a rotor located at each wing tip. The rotors can be rotated to permit conversion from the helicopter mode to the airplane mode and vice versa, the wing remaining fixed.

The concept was first proposed by Bell Helicopter engineers during World War II, and it evolved into a first prototype in 1955, designated the XV-3 [1]. In 1977, the NASA/Army/Bell XV-15, a 13,000 lb experimental tilt rotor aircraft, flew for the first time in a research program that continues to today. The usefulness of the tilt rotor aircraft is evidenced in the recent development of the V-22 Osprey for the U.S. Armed Forces by a Bell Helicopter Textron/Boeing Vertol team. The V-22 is a multi-service, multi-mission tilt rotor aircraft. It has a vertical take-off weight of 47,500 lb and is capable of transporting up to 40 passengers.

The unique features of the tilt rotor can also be exploited as a civil transport in the city-center to city-center commuter market or as a feeder to hub airports. The need for such a mode of transport will certainly increase as community real estate prices continue to increase, making new airport construction prohibitively expensive, driving new airport locations further away from large population densities.

The tilt rotor concept offers several considerable advantages over the rival tilt wing concept (in which the rotors and wing both rotate in the transition from helicopter to airplane mode and back). Wing tilt requires additional mechanical complexity and resulting increased structural weight to support the higher concentrated wing/fuselage junction loads. The tilt rotor concept also offers much greater controllability while hovering in gusty wind or cross-wind conditions.

A major limitation of the tilt rotor configuration, however, is the aerodynamic download imposed on the wing by the rotor flowfield when hovering. Because the wing is fixed, the rotor flow, in hover, hits the wing at 90 degrees. The download force on the wing has been measured and can be as large as 10 - 15 percent of the total rotor thrust [2,3]. Assuming the payload-carrying capability to be about 25% of gross take-off weight, complete elimination of the download could increase the effective payload by over 50%. The need for a thorough understanding of, and the eventual reduction of, wing download, then, is the major impetus driving this theoretical study on tilt rotor flowfields.

Study of the three-dimensional wing/rotor interaction, in hover, therefore, is the primary focus of this work. The flowfield about a tilt rotor configuration is very complicated. The rotor, typically located less than a wing chord above the wing, induces a flow which is closely coupled to the flow about the wing. There exists a large region of nearly-stagnated flow on the wing upper surface and a large region of unsteady, turbulent, separated flow below the wing. The flow over the wing upper surface is highly three-dimensional. Near the wing tip, the flow over the wing is essentially chordwise. Further inboard, the flow becomes increasingly spanwise. Due to symmetry of a hovering tilt rotor, the spanwise flow from both wings meets at the vehicle centerline and is redirected upwards. Some of this rising column of air is re-ingested by the rotor thus creating a large-scale recirculation pattern which reduces rotor performance. This flow pattern has been termed the "fountain effect". Refer

to Figure 1.1 for a simplified sketch of the main flow features about a V-22 in hover.

1.2 Previous Work

1.2.1 Experimental Work

Flight test of the XV-15 [1,4] has yielded quantitative estimates of hover performance including download as a function of flap angle. Figure 1.2 shows the download (DL) normalized by the rotor thrust (T) plotted as a function of flap angle. Flight test results are compared to estimates from a semi-empirical theory by Felker and Light [2] . To better study the nature of the tilt rotor flowfield itself, the flexibility and control offered by wind tunnel testing is required. McCroskey et al. [5] measured the drag of two-dimensional models of the XV-15 airfoil with various flap and leading edge configurations. They found that the drag on the airfoil in a freestream flow at -90 degrees was very sensitive to not only flap angle but also the surface curvature distribution on the upper surface near the leading edge. Lowering flap reduces the frontal area thereby reducing the download. A flat plate has a 2-D drag coefficient about twice that of a circular cylinder. Increasing airfoil thickness and camber, then, which tend to make the airfoil less like a flat plate and more like a circular cylinder or ellipse, reduces the download.

Maisel et al. [6] continued this 2-D experimental effort by examining the effects of several different airfoil, flap, and leading edge configurations on the download.

Boeing has tested a powered tilt rotor model whose basic geometry was that of a 0.15 scale V-22 Osprey. Some results of this test are reported in reference [7].

Results from model tests of tilt rotor hover and wing/rotor interaction by NASA have been reported in references [1,2,3]. Large-scale tests involving a 0.658 scale V-22 rotor and wing as well as small-scale tests of a 0.16 scale S-76 helicopter rotor and a model wing were carried out at the Outdoor Aerodynamic Research Facility

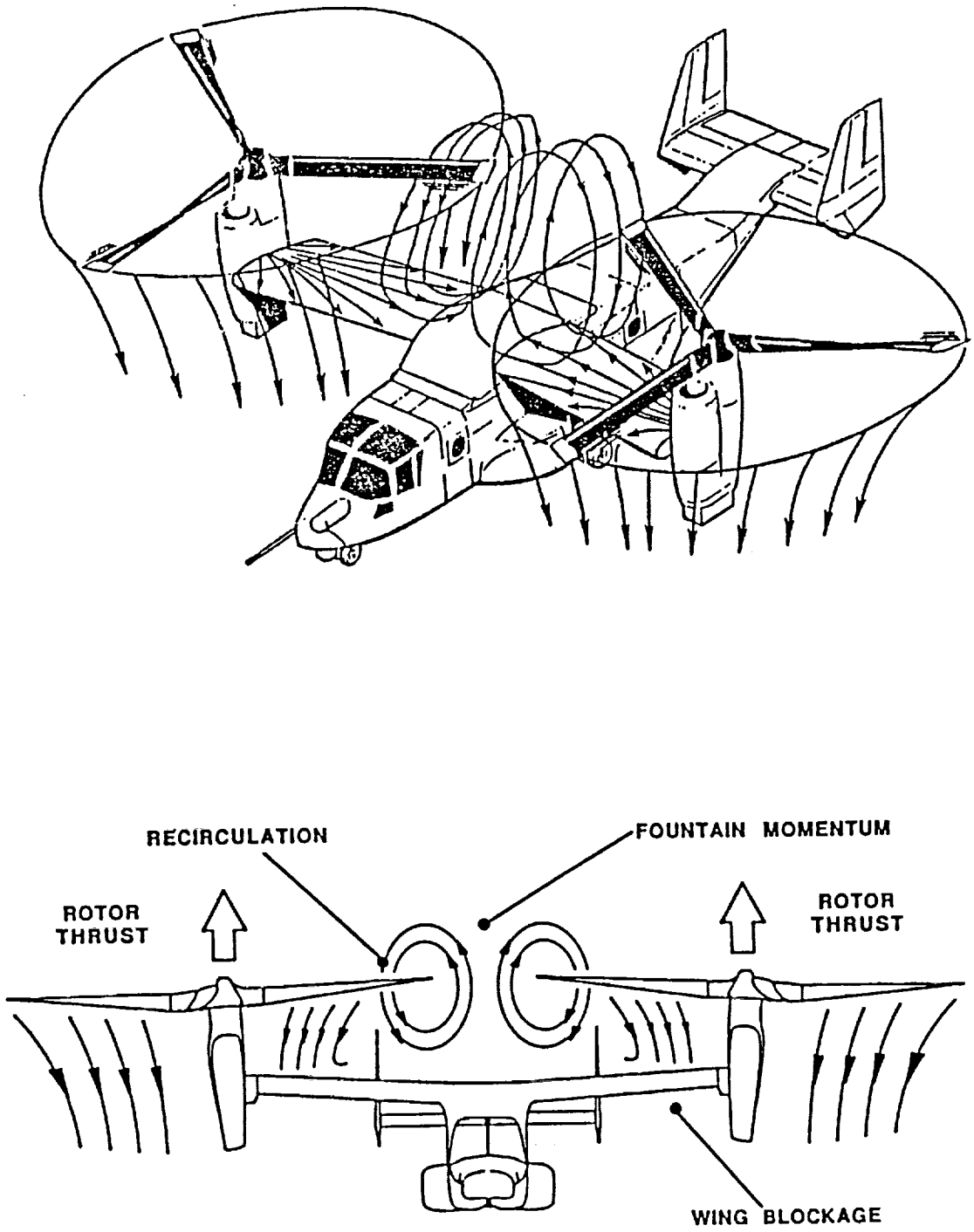

Figure 1.1: Sketch of the V-22 in hover, showing the main flow features.

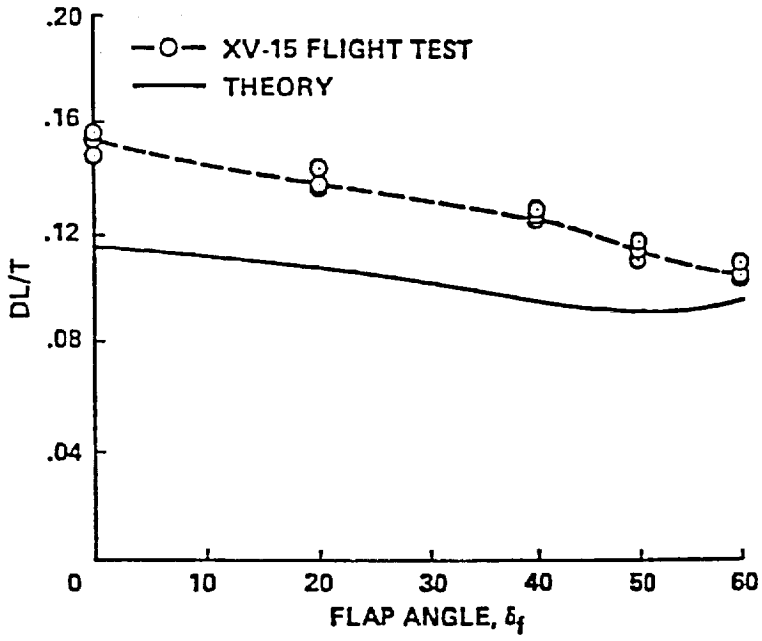

Figure 1.2: Effect of flap angle on download (Ref. [2]).

(OARF) at NASA Ames Research Center. These tests provided flow visualization of the complicated flowfield as well as wing pressure measurements and estimates of wing download and rotor performance. A clearer picture of the flowfield was obtained. The gradual transition from near-2-D flow on the outboard section of the wing to near-spanwise flow on the inboard region, and the fountain effect were observed.

Because the static pressure in separated flow is generally somewhat less than ambient pressure, a download suction force on the wing lower surface contributes to the total download. By energizing the boundary layer using tangential blowing on the upper surface near the leading edge (where the flow is close to separating) the separation location can be further extended around the leading edge to the lower surface thereby reducing the chordwise extent of the of the separated flow region below the wing and significantly reducing the download. This effect was observed in the experimental work described in [2] using the 0.16 scale model and wing with elliptic airfoil section with blowing slots. Figure 1.3 shows typical surface pressure

distributions on a circulation control airfoil with and without blowing in a rotor-induced -90 degree slipstream.. The slots were located at 3% and 97% chord, the former blowing towards the leading edge, the latter towards the trailing edge. It was found that particularly the leading edge slot was very effective in controlling the location of separation and in reducing the download.

A more detailed set of tests similar to those described above, scheduled for the Fall of 1989, will soon provide even more information. A 0.18 scale V-22 rotor and both a V-22 model wing and an XV-15 wing with blowing slots will be tested. This experimental research effort will provide a means of direct comparison with the computational results obtained in this theoretical study, whose preliminary results are reported here.

1.2.2 Theoretical Work

The theoretical prediction of tilt rotor flows and of download is very difficult because of the complexity of the flowfield. The rotor wake is an unsteady, three-dimensional flow with regions of concentrated vorticity (rotor tip vortices). The rotor blades themselves see highly compressible flows, and beneath the wing there exists a large region of unsteady, turbulent, separated flow. Accurate, simultaneous prediction of all these flow features still lies beyond the state of the art. Simplifications must be made to render the problem tractable.

References [8,9] describe the application of a low-order panel method to the tilt rotor problem. The rotor was modeled using source singularities and the rotor wake was represented by a time-averaged cylindrical vortex sheath comprised of quadrilateral doublet panels. A blade element model of the rotor feeds time-averaged loading as a function of radial and azimuthal location to the panel code which contains a model of the wing. The wing was modeled simply as a cambered plate using a lattice of doublet singularities. Many of the overall flow features were predicted using this

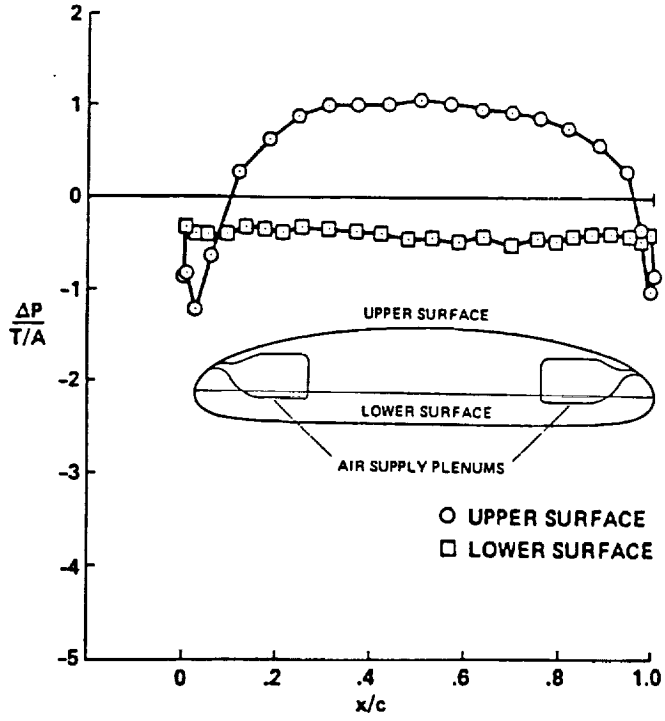

(a) blowing off, P_p/P_{atm} = 1.00.

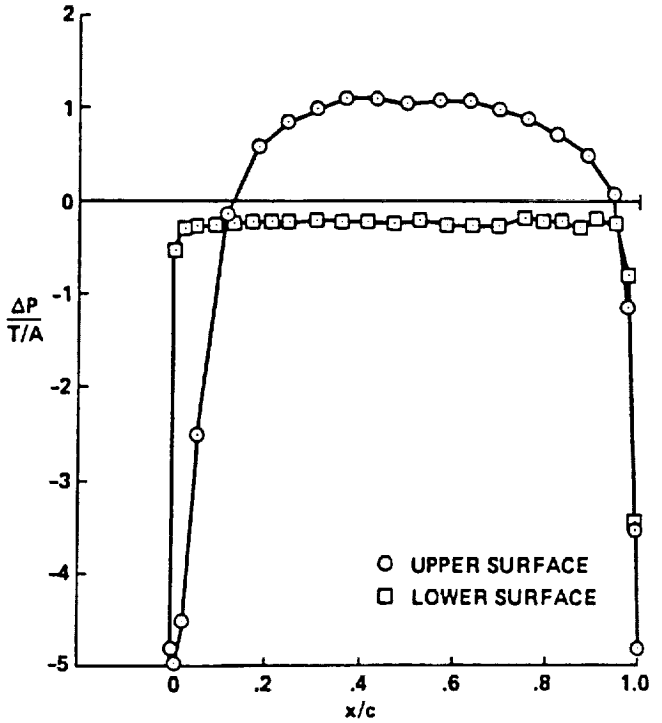

(b) blowing on, P_p/P_{atm} = 1.09.

Figure 1.3: Typical surface pressure distributions on a circulation control airfoil in hover mode with and without blowing.

method. Quantitative results, however, because of the nature of the equations solved (Laplace's equation) must be viewed with caution as separated flows cannot be accurately predicted with this formulation. As found in the experimental work described in reference [5], the separation location is very sensitive to leading edge curvature and thickness. These important effects cannot be accurately predicted using a panel method. Download, which is dependent on viscous effects, can only be accurately predicted using an analysis which incorporates the effect of viscosity.

References [5,10] describe discrete-vortex seeding methods to calculate the unsteady, 2-D flow around an airfoil at an angle of incidence of -90 degrees. In reference [5], the wing is immersed in a freestream flow. In reference [10], to study rotor/wing interaction, a rotor is modeled using constant strength doublet panels which induce a normal velocity distribution. Since no integral boundary layer calculation was coupled with the potential flow calculation, boundary layer growth and separation location were not predicted. Separation location was specified and a uniform base pressure on the wing lower surface was assumed. The methods predicted the upper surface pressures fairly well but obviously were incapable of accurately calculating the lower surface pressure. Since the flow over the tilt rotor wing is highly three-dimensional, two-dimensional analyses such as these are of limited usefulness.

Recent developments in numerical algorithms and in computer speed and memory capability have made tractable the solution of the Euler and Navier-Stokes equations for increasingly complicated flows. However, only very few attempts at the calculation of rotor flows have so far been made using the latest computational fluid dynamics (CFD) techniques.

Quasi-steady solutions of a 2-bladed rotor in hover have been obtained by Srinivasan and McCroskey [11] using a flux-split, approximately-factored, implicit algorithm to solve the unsteady, thin-layer Navier-Stokes equations. The computation of the concentrated vortices shed from the rotor tips is affected adversely by nu-

merical diffusion due to insufficient grid density beneath the rotor. Therefore, the effect of the rotor wake, and in particular, the induced downwash, must be estimated empirically in order to obtain reasonable results for lifting cases.

The same authors in reference [12] presented their results of airfoil/vortex interaction in two-dimensions. They describe a method where the structure of the vortex is prescribed, but its path in space is allowed to develop as part of the solution. Using this approach, they were able to simulate the effect of a shed tip vortex on a section of the following rotor blade.

Roberts [13] combined an unsteady Euler solver with a wake model for a two-bladed hovering rotor. The bound circulation distribution along the span of each rotor blade was determined from the Euler solution and used to set the strength of the wake vortices.

McCroskey and Baeder [14] estimated that in order to calculate two revolutions of a two-bladed rotor above a simple fuselage using a typical, implicit, thin-layer Navier-Stokes code with algebraic eddy-viscosity modeling of turbulence, a 100 megaflop computer would require 40 CPU hours and 30 million words of memory (or 4 hours of CPU for a one gigaflop machine). Routine calculations of 3-D rotorcraft flows including detailed modeling of the rotor blades will remain elusive for some time.

Rajagopalan and Mathur [15] modeled a three-dimensional rotor in forward flight using a distribution of momentum sources added to the steady, incompressible, laminar Navier-Stokes equations. Rotor geometry and blade sectional aerodynamic characteristics were incorporated into the evaluation of the source terms. Their results represent a time-averaged solution. In complexity, this method lies between an actuator disk representation and a CFD computation of the individual blades.

1.3 Current Approach

Despite the research efforts of the past several years, gaps in our fundamental understanding of the tilt rotor flowfield remain. It is the objective of this current work to model the tilt rotor flowfield as accurately as present computational tools allow. Computer resources and solution algorithms have evolved, during the past several years, to the point where the solution of the thin-layer Navier-Stokes equations about a simplified tilt rotor configuration comprised of wing and rotor model is technically feasible. Since the modeling of the flow about the individual rotor blades remains such a complex task and tremendous computational drain, and since the primary interest here is wing download prediction and not detailed rotor simulation, the rotor in this study, is modeled as an actuator disk. The loads from the blades are averaged over the entire rotor disk area. The viscous flow around the airfoil, however, is accurately predicted by defining a suitable grid. A multiple zone approach is used to incorporate the effects of the rotor. Empirical data or, in this case, a momentum theory/blade element analysis is used to estimate the average radial distribution of axial and swirl velocities, and the pressure rise across the rotor disk (which are required for the CFD calculation).

The theory and numerical method, grid generation, development of boundary conditions, and preliminary results obtained, will all be discussed in greater detail in the chapters to follow.

Chapter 2

Governing Fluid Dynamic Equations and Solution Method

2.1 General Comments

The work described in this report involves the numerical solution of the three-dimensional Navier-Stokes equations. It is assumed that there are no body forces (eg. gravity effects are not important) and there is no heat addition or removal. The thin-layer approximation, described later, is applied. It assumes that the viscous forces are confined to a small region near the wing surface. The solution method, in the form in which it is applied here, was formulated by Fujii and Obayashi [16,17,18]. It is suitable for subsonic, transonic, and supersonic flow calculations. Although the solution method is implicit, the boundary conditions are applied explicitly. This allows easier application of the code to a wide variety of geometries.

The general formulation is outlined in the following sections. Greater detail can be found in references [16,17,18,19].

2.2 Governing Equations

The Navier-Stokes equations are the most basic continuum-representation of fluid dynamic flows. To ensure proper shock capturing (in transonic flow, for example), i.e. to accurately predict shock strength and location, the three-dimensional Navier-

Stokes equations are written and solved in strong conservation law form where the dependent variables are expressed in the form of spatial gradients. These equations can be seen in several different references. See, for example, reference [19]. To convert them to a more useful form for computational purposes, the equations are manipulated somewhat. This is described below.

The equations are non-dimensionalized by dividing the density ρ by the freestream density ρ_∞, the velocity components u, v, and w by the freestream speed of sound a_∞, and the total energy per unit volume e by $\rho_\infty a_\infty^2$. Conforming to the normal convention, u is in the downstream (x) direction, v is in the spanwise (y) direction, and w is in the vertical, upwards (z) direction. The coefficient of viscosity is normalized by μ_∞ and the time is normalized by c/a_∞ where c is the wing chord. Applying this non-dimensionalization to the Navier-Stokes equations results in a term containing the expression $(\rho_\infty a_\infty c)/\mu_\infty$. Introducing the definition of Mach number, $M_\infty = u_\infty/a_\infty$ where $u_\infty = \sqrt{u^2+v^2+w^2}\Big|_\infty$, then it is seen that this expression equals Re/M_∞ where $Re = (\rho_\infty u_\infty c)/\mu_\infty$.

Next, the Navier-Stokes equations are transformed from Cartesian coordinates to general curvilinear coordinates. This makes the formulation independent of the body geometry thereby easing the specification of the boundary conditions. It also allows for straight-forward application of the thin-layer assumption later. In addition, since the physical domain is transformed into the computational domain which is a rectangular box with a uniformly-spaced mesh, then standard differencing schemes can be used for the derivatives. The coordinate transformation is defined by:

$$\begin{aligned} \tau &= t \\ \xi &= \xi(x,y,z,t) \\ \eta &= \eta(x,y,z,t) \\ \zeta &= \zeta(x,y,z,t) \end{aligned} \tag{2.1}$$

where t represents the time independent variable. The airfoil surface is transformed to the ξ-direction, the spanwise direction is transformed to η, and ζ is roughly normal to the wing surface. The governing equations must, correspondingly, be transformed from the physical domain (x, y, z) to the computational domain (ξ, η, ζ). Details of this transformation procedure can be found in references [20,21]. By writing the transformation in terms of spatial derivatives and applying the chain rule, a transformation Jacobian, J, and several identities called metrics can be defined as follows:

$$J = 1/\det \begin{vmatrix} x_\xi & x_\eta & x_\zeta \\ y_\xi & y_\eta & y_\zeta \\ z_\xi & z_\eta & z_\zeta \end{vmatrix} \tag{2.2}$$

where $x_\xi = \partial x/\partial \xi$, etc. i.e. all the above matrix elements area partial derivatives. They are evaluated numerically using second-order accurate differences. The metrics are:

$$\begin{aligned}
\xi_x &= J\,(y_\eta z_\zeta - y_\zeta z_\eta), & \zeta_x &= J\,(y_\xi z_\eta - y_\eta z_\xi) \\
\xi_y &= J\,(x_\zeta z_\eta - x_\eta z_\zeta), & \zeta_y &= J\,(x_\eta z_\xi - x_\xi z_\eta) \\
\xi_z &= J\,(x_\eta y_\zeta - x_\zeta y_\eta), & \zeta_z &= J\,(x_\xi y_\eta - x_\eta y_\xi) \\
\eta_x &= J\,(y_\zeta z_\xi - y_\xi z_\zeta), & \xi_t &= -x_\tau \xi_x - y_\tau \xi_y - z_\tau \xi_z \\
\eta_y &= J\,(x_\xi z_\zeta - x_\zeta z_\xi), & \eta_t &= -x_\tau \eta_x - y_\tau \eta_y - z_\tau \eta_z \\
\eta_z &= J\,(x_\zeta y_\xi - x_\xi y_\zeta), & \zeta_t &= -x_\tau \zeta_x - y_\tau \zeta_y - z_\tau \zeta_z
\end{aligned} \tag{2.3}$$

Note that for stationary grids (no body motion), the metric time derivative terms are zero.

Generally, the thin-layer approximation is applied to the Navier-Stokes equations to reduce the computational effort (particularly in three dimensions) to a manageable level. For the high Reynolds number flows which are typical of practical aerodynamic problems, the viscous effects are confined to a small region near the body surface and in the wake. Computer memory limitations usually necessitate concentrating

the available grid points near the surface of interest. This results in fine grid spacing normal and near to the surface and coarse grid spacing tangential to the surface. With this type of grid, even if the full Navier-Stokes equations were programmed, the viscous terms associated with the flux vectors along the body would not be resolved, and for most cases of interest, these terms are negligible anyway. Therefore, it is justifiable to eliminate from the calculation the viscous fluxes in the directions parallel to the surface, i.e. the ξ (chordwise) direction and the η (spanwise) direction. This is easy to do with the equations already transformed to the body-fitted computational domain. The thin-layer approximation is similar in philosophy but somewhat different than the assumptions in boundary layer theory. Less restrictive than boundary layer theory, the thin-layer approximation retains the normal momentum equation and allows pressure variation through the boundary layer.

The thin-layer approximation is less valid for low Reynolds number flows and in regions of large flow separation. This then is one of the major limitations of this method for studying the 3-D tilt rotor flowfield. Even if the full Navier-Stokes were solved, the limitations of the turbulence model in regions of extensive separation would contribute to inaccuracies in the computed flowfield in this region. The current approach, however, makes the calculation tractable and far superior to any method hitherto applied to this problem. The full 3-D Navier-Stokes solution is beyond the means of current practically-available computer power.

Applying the thin-layer approximation, then, the non-dimensional, 3-D Navier-Stokes equations in transformed curvilinear coordinates become:

$$\frac{\partial Q}{\partial \tau} + \frac{\partial E}{\partial \xi} + \frac{\partial F}{\partial \eta} + \frac{\partial G}{\partial \zeta} = \frac{M_\infty}{Re}\frac{\partial G_v}{\partial \zeta} \tag{2.4}$$

The Q vector contains the transformed conservative flow variables

$$Q = J^{-1}\begin{bmatrix} \rho \\ \rho u \\ \rho v \\ \rho w \\ e \end{bmatrix} \tag{2.5}$$

Note that the elements of the Q vector, as well as all flow variables referred to in subsequent discussions in this chapter, are non-dimensional quantities.

E, F, and G are vectors that contain the inviscid "Euler" terms:

$$E = J^{-1}\begin{bmatrix} \rho U \\ \rho u U + \xi_x p \\ \rho v U + \xi_y p \\ \rho w U + \xi_z p \\ U\,(e+p) - \xi_t p \end{bmatrix} \tag{2.6}$$

$$F = J^{-1}\begin{bmatrix} \rho V \\ \rho u V + \eta_x p \\ \rho v V + \eta_y p \\ \rho w V + \eta_z p \\ V\,(e+p) - \eta_t p \end{bmatrix} \tag{2.7}$$

$$G = J^{-1}\begin{bmatrix} \rho W \\ \rho u W + \zeta_x p \\ \rho v W + \zeta_y p \\ \rho w W + \zeta_z p \\ W\,(e+p) - \zeta_t p \end{bmatrix} \tag{2.8}$$

where p is the static pressure and U, V, and W are the contravariant velocity components that appear as a result of the coordinate transformation. They are defined below:

$$\begin{aligned} U &= \xi_t + \xi_x u + \xi_y v + \xi_z w \\ V &= \eta_t + \eta_x u + \eta_y v + \eta_z w \\ V &= \zeta_t + \zeta_x u + \zeta_y v + \zeta_z w \end{aligned} \tag{2.9}$$

The vector G_v contains the viscous terms retained after the application of the thin-layer approximation. It is given by

$$G_v = J^{-1}\frac{M_\infty}{Re}\begin{bmatrix} 0 \\ \zeta_x \tau_{xx} + \zeta_y \tau_{xy} + \zeta_z \tau_{xz} \\ \zeta_x \tau_{yx} + \zeta_y \tau_{yy} + \zeta_z \tau_{yz} \\ \zeta_x \tau_{zx} + \zeta_y \tau_{zy} + \zeta_z \tau_{zz} \\ \zeta_x \beta_x + \zeta_y \beta_y + \zeta_z \beta_z \end{bmatrix} \tag{2.10}$$

where

$$\tau_{xx} = -\frac{2}{3}\mu(u_x + v_y + w_z) + 2\mu u_x$$

$$
\begin{aligned}
\tau_{yy} &= -\frac{2}{3}\mu(u_x + v_y + w_z) + 2\mu v_y \\
\tau_{zz} &= -\frac{2}{3}\mu(u_x + v_y + w_z) + 2\mu w_z \\
\tau_{xy} &= \tau_{yx} = \mu\left(u_y + v_x\right) \\
\tau_{xz} &= \tau_{zx} = \mu\left(u_z + w_x\right) \\
\tau_{yz} &= \tau_{zy} = \mu\left(v_z + w_y\right) \\
\beta_x &= \frac{\gamma\mu}{Pr}\partial_x e_i + u\tau_{xx} + v\tau_{xy} + w\tau_{xz} \\
\beta_y &= \frac{\gamma\mu}{Pr}\partial_y e_i + u\tau_{yx} + v\tau_{yy} + w\tau_{yz} \\
\beta_z &= \frac{\gamma\mu}{Pr}\partial_z e_i + u\tau_{zx} + v\tau_{zy} + w\tau_{zz}
\end{aligned}
\tag{2.11}
$$

The internal energy per unit mass, e_i is

$$
e_i = \frac{e}{\rho} - \frac{(u^2 + v^2 + w^2)}{2}
$$

The Prandtl number Pr is defined as $Pr = c_p\mu/k$ where c_p is the specific heat at constant pressure and k is the coefficient of thermal conductivity. Also, γ is the ratio of specific heats. For air, at temperatures and pressures of interest here, $Pr = 0.72$ and $\gamma = 1.4$. Pressure is related to the conservative flow variables through the equation of state for a perfect gas

$$
p = (\gamma - 1)\left[e - \frac{\rho}{2}\left(u^2 + v^2 + w^2\right)\right] \tag{2.12}
$$

To evaluate the spatial derivatives of the Cartesian velocity components in Eq. 2.11, the chain rule is applied. For example,

$$
u_x = \xi_x u_\xi + \eta_x u_\eta + \zeta_x u_\zeta
$$

2.3 Turbulence Model

In order to resolve the turbulent eddies which contribute to a flow's turbulence level, an extremely tiny grid spacing and a huge number of points would be required.

For the solution of practical problems of interest to be feasible, a turbulence model is generally introduced which greatly reduces the number of grid points required in viscous regions. Based on a combination of theory and empiricism, turbulence models, although far from precise predictors of turbulence, do provide a means of modeling a real flow with a turbulent boundary layer.

For the purposes of this preliminary work, no turbulence model was incorporated. Only laminar flow calculations were performed because the main focus was on modification of the Navier-Stokes code for the tilt rotor problem, and on generation of suitable grids and boundary conditions.

A turbulence model proposed by Baldwin and Lomax [22] for conventional boundary layers and another for turbulent wall jets on curved surfaces proposed by Roberts [23] will be incorporated in the near future.

2.4 Numerical Algorithm

The solution technique employs an implicit, approximately factored, non-iterative method first developed by Beam and Warming [24]. Explicit methods suffer the disadvantage of having a severe restriction on time step size in order to maintain stability. This is particularly acute for Navier-Stokes solutions where, because of the relatively small scales associated with resolving the boundary layer, the partial differential equations are very stiff. Often, the steady-state solution is of principal interest, so being able to use large time steps to accelerate the rate of convergence is very important. Implicit methods are stable for relatively large time steps even for highly nonlinear equations such as the Navier-Stokes equations.

Applying the first-order accurate (in time) implicit Euler scheme to Eq. 2.4 results in

$$Q^{n+1} - Q^n + \Delta t \left(\frac{\partial E^{n+1}}{\partial \xi} + \frac{\partial F^{n+1}}{\partial \eta} + \frac{\partial G^{n+1}}{\partial \zeta} - \frac{M_\infty}{Re} \frac{\partial G_v^{n+1}}{\partial \zeta} \right) = 0 \qquad (2.13)$$

where $n+1$ is the time at which Q is desired, n is the previous time level at which

Q is known everywhere, and $Q^n = Q(n\Delta t)$.

Since the flux vectors E, F, G, and G_v are nonlinear functions of Q, then Eq. 2.13 is nonlinear in Q^{n+1}. In order for the method to be non-iterative, the nonlinear terms are linearized in time about Q^n by a Taylor series expansion such that

$$\begin{aligned} E^{n+1} &= E^n + A^n \Delta Q^n + O\left(\Delta t^2\right) \\ F^{n+1} &= F^n + B^n \Delta Q^n + O\left(\Delta t^2\right) \\ G^{n+1} &= G^n + C^n \Delta Q^n + O\left(\Delta t^2\right) \\ G_v^{n+1} &= G_v^n + M^n \Delta Q^n + O\left(\Delta t^2\right) \end{aligned} \tag{2.14}$$

Note that $\Delta Q^n = Q^{n+1} - Q^n$. Also, A^n, B^n, C^n, and M^n are the flux Jacobians. Expressions for these matrices can be found in reference [25].

In the Beam and Warming method, the alternating direction implicit (ADI) algorithm replaces the inversion of one huge matrix — which would be prohibitively expensive to compute — to the inversions of three block tridiagonal matrices, one for each direction. Efficient block tridiagonal inversion routines exist, making this algorithm a viable solution technique.

A linear constant coefficient Fourier stability analysis (assumes periodic boundary conditions) for the three-dimensional model wave equation shows a mild, unconditional instability for the Beam-Warming factored algorithm [26]. A small amount of artificial dissipation (also called "smoothing") is required to render the scheme stable. The most common procedure is to add fourth-order artificial dissipation to the explicit right hand side of the equation (see Eq. 2.15 below) and second-order dissipation to each of the three implicit one-dimensional block operators on the left hand side. Second-order implicit dissipation is used so as to keep the block implicit operators tridiagonal.

Applying the Beam-Warming scheme to Eq. 2.13 using the linearized expressions

for the flux vectors, Eqs. 2.14, the solution algorithm can be written as

$$\begin{aligned}
&\left[I + \Delta t\, \delta_\xi A^n - \Delta t\, \epsilon_I J^{-1} \nabla_\xi \Delta_\xi J\right] \left[I + \Delta t\, \delta_\eta B^n - \Delta t\, \epsilon_I J^{-1} \nabla_\eta \Delta_\eta J\right] \\
&\left[I + \Delta t\, \delta_\zeta C^n - \Delta t\, \frac{M_\infty}{Re} J^{-1} \delta_\zeta M^n J - \Delta t\, \epsilon_I J^{-1} \nabla_\eta \Delta_\eta J\right] \Delta Q^n \\
&\qquad = -\Delta t \left[\delta_\xi E^n + \delta_\eta F^n + \delta_\zeta G^n - \frac{M_\infty}{Re} \delta_\zeta G_v^n\right] \qquad (2.15) \\
&\qquad\quad -\Delta t\, \epsilon_E J^{-1} \left[(\nabla_\xi \Delta_\xi)^2 + (\nabla_\eta \Delta_\eta)^2 + (\nabla_\zeta \Delta_\zeta)^2\right] J\, Q^n
\end{aligned}$$

In the above notation,

$$[I + \Delta t\, \delta_\xi A^n]\, \Delta Q^n = \Delta Q^n + \Delta t\, \delta_\xi \left(A^n \Delta Q^n\right)$$

Note that I is the identity matrix, δ is a central difference operator, and ∇ and Δ are backward and forward difference operators, respectively. ϵ_I and ϵ_E are constants that control the magnitude of artificial dissipation introduced in the scheme on the implicit side (left hand side) and on the explicit side (right hand side) of Eq. 2.15, respectively.

The algorithm is said to be in "delta form". For steady-state solutions ,$\Delta Q^n \rightarrow 0$, and the solution is independent of the choice of operators on the left hand side of Eq. 2.15. The algorithm is first-order accurate in time. Since second-order spatial differences are used on the implicit side, the method is second-order in space. For converged, steady-state solutions, when the implicit side (left hand side) of the equation approaches zero, and if fourth-order differencing is used on the explicit (right hand side terms), then the method becomes fourth-order accurate in space.

Most of the computational effort involved in an implicit algorithm such as the one outlined above is associated with inverting the block tridiagonal matrices in each direction. Pulliam and Chaussee [27] suggested a way to diagonalize the blocks within the block tridiagonal matrices, thereby transforming them to scalar tridiagonal matrices which are much more efficient computationally to invert. Their approach is based on the fact that the flux Jacobians A, B, and C each have real eigenvalues

and a complete set of eigenvectors. This means that the Jacobian matrices can be diagonalized by similarity transformations as indicated below:

$$\Lambda_\xi = T_\xi^{-1} A T_\xi, \quad \Lambda_\eta = T_\eta^{-1} B T_\eta, \quad \Lambda_\zeta = T_\zeta^{-1} C T_\zeta$$

where, for clarity, the superscript n has been dropped from the flux Jacobians. Λ_ξ, Λ_η, and Λ_ζ are diagonal matrices containing the eigenvalues of matrices A, B, and C, respectively. T_ξ, T_η, and T_ζ are similarity transformation matrices. Expressions for the above matrices can be found in references [26,27].

For simplicity, looking at only the ξ-direction, the Beam-Warming's ADI implicit operator (see Eq. 2.15) can be written in the diagonal form as

$$\begin{aligned} & I + \Delta t\, \delta_\xi A + \Delta t\, \epsilon_I J^{-1} \nabla_\xi \Delta_\xi J \\ & \quad = T_\xi T_\xi^{-1} + \Delta t\, \delta_\xi \left(T_\xi \Lambda_\xi T_\xi^{-1} \right) + \Delta t\, J^{-1} \epsilon_I \nabla_\xi \Delta_\xi J \\ & \quad \approx T_\xi \left[I + \Delta t\, \delta_\xi \Lambda_\xi + \Delta t\, J^{-1} \epsilon_I \nabla_\xi \Delta_\xi J \right] T_\xi^{-1} \end{aligned} \tag{2.16}$$

Moving T_ξ and T_ξ^{-1} outside of the difference operator δ_ξ introduces an error which renders the method at most first-order accurate in time [27]. For steady-state calculations, however, where the left hand side of Eq. 2.15 goes to zero as $\Delta Q^n \rightarrow 0$, the solution obtained using the diagonal algorithm will be identical to that obtained from the original Beam-Warming ADI scheme since the right hand side is identical for both methods.

Fujii, Obayashi, and Kuwahara [16,17,18] introduced a further modification to the left hand side operators that reduces the tridiagonal matrix — obtained after the diagonalization described above — to a product of a lower and an upper bidiagonal matrix, thereby reducing the computational effort even more. This is possible by employing the flux vector splitting technique introduced by Steger and Warming in reference [28], and by using a diagonally dominant factorization first proposed in reference [29]. These modifications are outlined below.

The central differencing of Eq. 2.16 can be decomposed into two one-sided differences by using the flux vector splitting technique. Continuing to look at the ξ-direction operator only, Eq. 2.16 can be re-written as

$$\begin{aligned} & I + \Delta t\, \delta_\xi A + \Delta t\, \epsilon_I J^{-1} \nabla_\xi \Delta_\xi J \\ & \quad \approx T_\xi \left[I + \nabla_\xi \Lambda_\xi^+ + \Delta_\xi \Lambda_\xi^- \right] T_\xi^{-1} \end{aligned} \tag{2.17}$$

with

$$\Lambda_\xi^\pm = \frac{\Delta t}{2} \left(\Lambda_\xi \pm |\Lambda_\xi| \right) \pm \Delta t\, \underline{J}^{-1} \epsilon_I J \tag{2.18}$$

where Λ_ξ^+ contains all the positive eigenvalues and Λ_ξ^- contains all the negative eigenvalues. Note that the positive-moving characteristics (eigenvalues) are backward differenced, and the negative-moving characteristics are forward differenced. This is required for numerical stability. $\underline{J}^{-1}$, the inverse of the Jacobian, is evaluated at the central point. Using first-order, three-point, upwind differencing (three-point differences offer greater numerical stability than two-point differences) for the ∇_ξ and Δ_ξ operators, Eq, 2.17 can be written as

$$\approx T_\xi \left[L_\xi + D_\xi + U_\xi \right] T_\xi^{-1} \tag{2.19}$$

where

$$\begin{aligned} L_\xi &= -\frac{8}{6} \Lambda_{j-1}^+ + \frac{1}{6} \Lambda_{j-2}^+ \\ D_\xi &= I + \frac{7}{6} \left(\Lambda_j^+ - \Lambda_j^- \right) \\ U_\xi &= \frac{8}{6} \Lambda_{j+1}^- - \frac{1}{6} \Lambda_{j+2}^- \end{aligned} \tag{2.20}$$

where the subscript j is the grid point index in the ξ-direction.

Applying diagonally dominant factorization (refer to [29]),

$$L_\xi + D_\xi + U_\xi = \left(L_\xi + D_\xi \right) D_\xi^{-1} \left(D_\xi + U_\xi \right) + O\left(\Delta t^2 \right) \tag{2.21}$$

This can be shown by examining Eqs. 2.18 and 2.20 and noting that D_ξ is of order 1 and L_ξ, U_ξ are of order Δt. Substituting Eq. 2.21 into Eq. 2.19, Eq. 2.17 becomes

$$I + \Delta t\, \delta_\xi A + \Delta t\, \epsilon_I \nabla_\xi \Delta_\xi J$$
$$\approx T_\xi \left(L_\xi + D_\xi\right) D_\xi^{-1} \left(D_\xi + U_\xi\right) T_\xi^{-1} \tag{2.22}$$

The block tridiagonal system of the left hand side of Eq. 2.16 has been transformed to matrix multiplications and the product of the lower scalar bidiagonal matrix $(L_\xi + D_\xi)$ and the upper scalar bidiagonal matrix $D_\xi^{-1}(D_\xi + U_\xi)$. The same analysis is carried out for the η-direction and a slightly modified analysis is performed in the ζ-direction.

The viscous flux Jacobian M^n is not diagonalizable by the similarity transformations T_ξ and T_ξ^{-1} and, therefore, the ζ-direction implicit operator of Eq. 2.15 cannot be reduced to diagonal form. To retain the diagonalization in all three directions (and not incur the computation penalties associated with not simplifying the block tridiagonal operator in the ζ-direction), the viscous flux Jacobian M^n is simply neglected. Pulliam [26] , using the unsplit diagonalized method, compared results obtained with and without the implicit viscous flux Jacobian. He found that neglecting this term actually yielded the most efficient steady-state solutions. Pulliam and Steger [32] employ this method for steady viscous flows and convection dominated unsteady flows. Guruswamy [30,31] , using this same numerical algorithm (ignoring the implicit viscous flux Jacobian) for both the Euler and Navier-Stokes equations, obtained good results for unsteady aerodynamic and aeroelastic calculations.

In order to maintain stability of the Fujii/Obayashi method with the thin-layer viscous terms retained on the explicit, right hand side of the equation, the diagonal matrix of eigenvalues, Λ_ζ, of the inviscid flux Jacobian matrix ,C^n, is modified (see references [16,18]) as indicated below (compare with Eq. 2.18, for example):

$$\Lambda_\zeta^{\pm} = \frac{\Delta t}{2}\left(\Lambda_\zeta \pm |\Lambda_\zeta|\right) \pm \Delta t\, \underline{J}^{-1} \epsilon_I J \pm \nu I$$

where

$$\nu = \frac{2\mu\sqrt{\zeta_x^2 + \zeta_y^2 + \zeta_z^2}}{\frac{Re}{M_\infty}\rho\,\Delta\zeta}$$

where, in the computational domain, $\Delta\xi = \Delta\eta = \Delta\zeta = 1$.

Finally, the present scheme can be summarized as follows,

$$\begin{aligned} &T_\xi\,(L_\xi + D_\xi)\,D_\xi^{-1}\,(D_\xi + U_\xi)\,T_\xi^{-1}T_\eta\,(L_\eta + D_\eta)\,D_\eta^{-1}\,(D_\eta + U_\eta)\,T_\eta^{-1}T_\zeta \\ &(L_\zeta + D_\zeta)\,D_\zeta^{-1}\,(D_\zeta + U_\zeta)\,T_\zeta^{-1}\,\Delta Q^n \\ &\qquad = -\Delta t\left[\delta_\xi E^n + \delta_\eta F^n + \delta_\zeta G^n - \frac{M_\infty}{Re}\delta_\zeta G_v^n\right] \\ &\qquad\quad -\Delta t\,\epsilon_E J^{-1}\left[(\nabla_\xi\Delta_\xi)^2 + (\nabla_\eta\Delta_\eta)^2 + (\nabla_\zeta\Delta_\zeta)^2\right] J\,Q^n \end{aligned} \tag{2.23}$$

Analytical expressions for $T_\xi^{-1}T_\eta$ and $T_\eta^{-1}T_\zeta$ and their inverses can be used to reduce the computational effort. They are presented in reference [27].

It is evident from the above equation that the inversion process has been reduced to one forward scalar sweep and one backward scalar sweep in each direction, and simple matrix multiplications.

2.5 Additional Features

To further enhance convergence speeds for steady-state calculations, a space varying time step size Δt can be specified. This modification can be very effective for typical grids that have a wide variation of grid spacing. By scaling Δt with grid spacing, a more uniform local Courant number (ratio of local time step to grid cell width multiplied by the characteristic velocity) can be maintained throughout the flowfield. Since the local transformation Jacobian, J, scales with the inverse of grid cell volume, the following has been found to work well (refer to [32]:

$$\Delta t = \frac{\Delta t|_{ref}}{1 + \sqrt{J}}$$

where $\Delta t|_{ref}$ is a fixed, inputted time step. Due to numerical approximations made to calculate the metrics, a computed freestream flow may be somewhat in error. To

remedy this problem, freestream subtraction is employed [33]. The freestream values of all the fluxes are calculated and subtracted from all the computed fluxes. This allows for recovery of the freestream condition without affecting the basic formulation.

Chapter 3

Grid Generation

3.1 General Philosophy

Grid generation is a very important aspect of computational fluid dynamics. The grid is the assembly of points at which the numerical solution to the relevant partial differential equations is found. To maintain solution accuracy, the grid should possess a smooth distribution of points (refer to [34]). Also, the grid (or mesh) and the distribution of points must be compatible with the fluid dynamics equations being solved and the particular flowfield expected.

As discussed in Section 2.2, the thin-layer approximation is made so as to limit the computer storage requirements to a manageable level. The viscous fluxes normal to the surface are dominant. In order to resolve this important contribution, the grid spacing must be very fine in a direction normal to the surface. Grid spacing can be much coarser along the surface where the far less significant tangential viscous fluxes need not be resolved. In addition, grid points must be clustered in regions where relatively large flow gradients are anticipated. For example, the wing leading edge and trailing edge as well as the mid-chord regions for $\alpha = -90°$ flow require grid point concentration. Figure 5.1 is an example of the grid generated for a freestream flow computation about the V-22 airfoil at an angle of incidence of -90 degrees. There are 47 points in the circumferential direction around the airfoil surface, three of which overlap to ease implementation of the periodic boundary conditions (refer

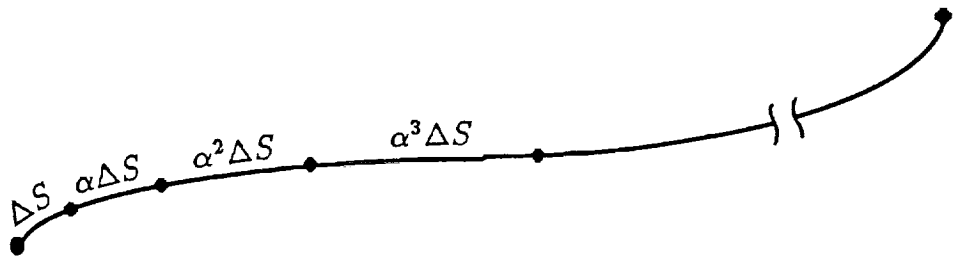

Figure 3.1: Exponential grid point stretching applied to an arbitrary curve.

to Section 4.2 for a further discussion of periodic boundary conditions). There are 33 points in the direction normal to the airfoil surface.

To obtain the desired clustering of grid points on a body surface and in the mesh interior for algebraically-defined grids, extensive use is made of an exponential type of stretching. If a distribution of N points is desired along a curve of specified length S, and the arc length between the first two points is specified to be ΔS, then an expression for the total length can be written as (refer to Figure 3.1) :

$$\begin{aligned} S &= \Delta S + \alpha\Delta S + \alpha^2\Delta S + \alpha^3\Delta S + \cdots \\ &= \Delta S \sum_{k=0}^{N-2} \alpha^k \end{aligned}$$

Defining a function f where

$$f = S - \Delta S \sum_{k=0}^{N-2} \alpha^k$$

then an iterative root finding procedure such as the Newton-Raphson method is used to determine the value of α that satisfies $f = 0$ within a desired tolerance. This method can easily be extended to a distribution of points with exponential stretching in both directions, i.e. a different ΔS is specified at both ends of the interval.

To generate a mesh for a 2-D calculation, five identical 2-D grids were stacked parallel to each other. This is required because the Navier-Stokes code employs

a fourth-order accurate 5-point spatial numerical differencing. The computational results are then referred to as " pseudo 2-D " as they are essentially 2-D in character although they are generated by a 3-D code. This is made possible by proper application of symmetry boundary conditions at both ends of the mesh (refer to Section 4.2).

For actual 3-D cases, 2-D grids are generated at many spanwise stations along the wing and beyond the wing tip, and stacked in parallel.

3.2 Elliptic Grid Generation

To ensure smooth grid point distributions on the interior of a 2-D mesh, an elliptic grid solver can be employed. It is well-suited to the types of grids employed in this study. Because of the symmetry of the 2-D flowfield at a given station of the tilt rotor wing in hover, an O-grid is more suitable than either a C-grid or an H-grid. The O-grid is so named because of the way the grid lines encircle the airfoil.

The elliptic grid generation scheme was first proposed by Thompson, Thames, et al. in references [35,36]. It requires specification of grid point locations along the boundary – in this case, both the inner boundary (airfoil surface) and the outer boundary. The solution algorithm is outlined below.

The Poisson equations are used to generate a boundary-fitted, curvilinear 2-D grid:

$$\begin{aligned} \xi_{xx} + \xi_{yy} &= P(\xi, \eta) \\ \eta_{xx} + \eta_{yy} &= Q(\xi, \eta) \end{aligned}$$

where (ξ, η) represent coordinates in the computational domain, (x, y) represent coordinates in the physical domain, and P and Q are source terms which control the grid point spacing in the mesh interior. The computational domain is rectangular and the grid points within it are evenly-spaced. To simplify the evaluation of the

derivatives and to ease the specification of the boundary conditions, the above equations are transformed to, and solved in, the computational domain. To do this, the roles of the independent and dependent variables are interchanged, and the equations become

$$\begin{aligned} \alpha x_{\xi\xi} - 2\beta x_{\xi\eta} + \gamma x_{\eta\eta} &= -J^2 (P x_\xi + Q x_\eta) \\ \alpha y_{\xi\xi} - 2\beta y_{\xi\eta} + \gamma y_{\eta\eta} &= -J^2 (P y_\xi + Q y_\eta) \end{aligned} \tag{3.1}$$

where

$$\begin{aligned} \alpha &= x_\eta^2 + y_\eta^2 \\ \beta &= x_\xi x_\eta + y_\xi y_\eta \\ \gamma &= x_\xi^2 + y_\xi^2 \\ J &= x_\xi y_\eta - x_\eta y_\xi \end{aligned}$$

All derivatives are approximated using standard second-order accurate finite differences. The spatial increments $\Delta\xi$ and $\Delta\eta$ can, without any loss in generalization, be assumed to be constant everywhere and equal to 1. The grid point locations on the boundary must be specified, and an initial guess for the interior grid values must be made. Any number of standard relaxation schemes can be used to solve the system of two elliptic equations. Here, a fully implicit scheme – an alternating direction implicit (ADI) scheme – constructed using approximate factorization to convert the solution process to two one-dimensional inversions is employed. The solution method is discussed in more detail in reference [37].

This method with $P = Q = 0$ provides no control over the grid point spacing near a boundary. The grid points tend to be pulled away from the surface by the Laplacian elliptic solver. Sorenson and Steger [38] developed a technique for defining P and Q such that the angle at which the $\xi = constant$ grid lines intersect the boundary, as well as the distance between the boundary and the first off-boundary grid point on

these grid lines, could be specified. In this way, grids having a very fine grid spacing near surfaces (for viscous calculations) can be generated. Also, orthogonality of the grid at the boundaries can be specified, if desired.

In this current study, the elliptic grid solver has been used to generate the grids for the 2-D and 3-D freestream calculations. Since Sorenson and Steger's boundary control technique has not as yet been implemented (i.e. $P = Q = 0$), post-processing in the form of exponential stretching was employed to obtain the desired grid density in the boundary layer region.

For the wing/rotor interaction computations, a grid with a flat outer boundary in the plane of the rotor is desired so as to enable an easier and a more accurate implementation of the boundary conditions that correspond to the rotor. An outer grid is then defined to encircle the inner zone. See , for example, Figures 5.20 and 5.21. These grids have been generated purely algebraically. Elliptic grid smoothing has not as yet been applied to the rotor/wing meshes.

Chapter 4

Boundary Conditions

4.1 General Remarks

The finite difference solution of the Navier-Stokes equations requires specification of boundary conditions on all domain boundaries. In the numerical method employed in this study (described in Chapter 2), the boundary conditions are applied explicitly, i.e. the flow variables at the boundaries are evaluated at the time level preceding that at which the implicit solution on the mesh interior is found. This permits greater flexibility in applying the boundary conditions to a variety of geometries and flow situations. At all grid points located on the mesh boundaries, each of the five flow parameters that make up the vector of conserved quantities, Q, must be updated explicitly – either by specifying them or by extrapolating from computed interior values. Referring then to the definition of Q in Section 2.2, the density ρ, the three components of mass flux ρu, ρv, and ρw, and the total energy per unit volume, e, must all be updated at each time step.

Determination of the boundary conditions representative of a lifting rotor require a separate analysis and will be discussed in a later section. First, those boundary conditions not pertaining to the rotor will be described.

4.2 Non-Rotor Boundary Conditions

At grid points on the wing surface, for viscous (Navier-Stokes) calculations the no-slip boundary condition is imposed, i.e. all components of velocity are zero ($u = v = w = 0$). Inviscid computations can also be performed using the present computer code by omitting all viscous terms, i.e. the G_v flux vector, and by applying the inviscid boundary condition on the wing – zero normal velocity. In the rectangular computational domain, this condition is easily satisfied by setting the contravariant velocity component normal to the surface, W, to zero.

The pressures on the wing surface are found by solving the normal momentum equation (refer to [33,34]). The normal momentum equation is derived by taking the dot product of the vector comprised of the transformed x-, y-, and z- momentum equations, and the unit normal vector, $\vec{n}$. The viscous effects are assumed to have an insignificant effect on the pressure at the surface and are neglected (typical boundary layer assumption).

$$\left[x\text{–}mom\,\vec{i} + y\text{–}mom\,\vec{j} + z\text{–}mom\,\vec{k} \right] \cdot \vec{n} \;=\; normal\ momentum$$

where

$$\vec{n} = \frac{\nabla\vec{\zeta}}{\left|\nabla\vec{\zeta}\right|} = \frac{\zeta_x\vec{i} + \zeta_y\vec{j} + \zeta_z\vec{k}}{\sqrt{\zeta_x^2 + \zeta_y^2 + \zeta_z^2}}$$

From the momentum equations, it can be seen that the normal-momentum equation, at the body surface reduces to $\partial p/\partial n = p_n = 0$. Performing the above operations,

$$\begin{aligned} & p_\xi\left(\xi_x\zeta_x + \xi_y\zeta_y + \xi_z\zeta_z\right) + p_\eta\left(\eta_x\zeta_x + \eta_y\zeta_y + \eta_z\zeta_z\right) + p_\zeta\left(\zeta_x^2 + \zeta_y^2 + \zeta_z^2\right) \\ + \;& \rho U\left(\zeta_x u_\xi + \zeta_y v_\xi + \zeta_z w_\xi\right) + \rho V\left(\zeta_x u_\eta + \zeta_y v_\eta + \zeta_z w_\eta\right) \\ = \;& p_n\sqrt{\zeta_x^2 + \zeta_y^2 + \zeta_z^2} \end{aligned}$$

where $U = V = 0$ for viscous flow calculations. p_ζ can be approximated by second-order one-sided differences and p_ξ and p_η by second-order central differences at the

surface. Re-arranging the equation, and applying approximate factorization, results in an implicit solution algorithm for p at the surface which involves two one-dimensional tridiagonal inversions - one in the ξ-direction and the other in the η-direction. Obtaining surface pressures using the above method yields a more accurate and stable solution method than simply using zero-order extrapolation.

Once the surface pressures are known, assuming adiabatic conditions at the surface (i.e. no heat flux - zero normal temperature gradient), then the density is obtained by a zero-order extrapolation from the value at the nearest off-body point.

The final quantity required, the total energy per unit volume, e, is calculated directly from Eq. 2.12 using all previously-defined quantities.

Only one-half of the tilt rotor configuration is modeled due to the symmetry that exists in hover. Two parallel 2-D grid planes straddle the plane of symmetry and these grid points are used to specify the following symmetry boundary conditions

$$\begin{aligned} \rho_1 &= \rho_3 \\ (\rho u)_1 &= (\rho u)_3 \\ (\rho v)_1 &= -(\rho v)_3 \\ (\rho w)_1 &= (\rho w)_3 \\ e_1 &= e_3 \end{aligned} \tag{4.1}$$

This ensures that, at the centerline, there is no temperature gradient (assuming adiabatic conditions) or pressure gradient, and that the spanwise component of velocity is zero.

The 3-D Navier-Stokes code was modified to allow the computation of two-dimensional flows. Because fourth-order spatial differencing is used on the right hand side of Eq. 2.23, at least five parallel and identical 2-D grids are required. For "pseudo 2-D" calculations, then, symmetry conditions are also applied between grid planes 3 and 5. This ensures that the code effectively sees an infinitely long wing

having constant airfoil section.

On all outer boundaries other than the plane of symmetry, inflow or outflow boundary conditions are specified. The flow is essentially inviscid in these far-field regions. The Euler equations are hyperbolic partial differential equations. Applying a method of characteristics analysis to hyperbolic PDE's helps to determine the appropriate boundary conditions for inflow and outflow boundaries. For subsonic flow in three dimensions, four of the characteristic velocities are positive and the fifth one is negative. For a subsonic inflow boundary, then, four independent flow thermodynamic and kinematic flow properties should be specified, and one should be extrapolated from the interior of the flow domain. For a subsonic outflow boundary, on the other hand, only one property should be specified and four extrapolated. For freestream calculations for flow at an angle of incidence of -90 degrees, inflow boundary conditions are applied at the grid points on the outer boundary that lie above the chord plane. Freestream Mach number and flow angle are specified. Also the pressure is set to be freestream ambient. The density is extrapolated from the interior using zero-order extrapolation. The outflow boundary is defined as those points on the outer boundary which lie below the chord plane. Here zero-order extrapolation from the nearest interior point is used for four flow properties. The pressure is specified and assumed to be again at freestream ambient.

The grid points of the O-grid along the airfoil surface (j index) wrap around the airfoil and overlap by three points. This couples the $j = 1$ and the $j = JMAX$ boundaries, which in the rectangular volume computational domain, are at opposite ends. The following periodic boundary conditions are then imposed, where the subscripts are for the j index:

$$q_1 = q_{JMAX-2}$$

$$q_{JMAX} = q_3$$

where q represents an element of the vector of conserved quantities, Q, and the above

is applied to all five elements. Also, for consistency,

$$q_2 = q_{JMAX-1}$$

is specified.

4.3 Modeling the Rotor

4.3.1 Approach

As discussed in Chapter 1, detailed modeling of individual rotor blades using CFD is a formidable task requiring computer resources that push the currently-available technology. Because the focus of this work is wing download, the problem is rendered more tractable by employing a simpler model for the rotor. The rotor is assumed to be an actuator disk. The combined position- and time- dependent effects of the blades on the flow are averaged. In the analysis presented here, radial variations in loading are permitted. On any given annular ring of the actuator disk, the load is assumed to be uniform.

A classical analysis of propellers/rotors is employed which combines axial and angular momentum conservation through the rotor disk with blade element strip theory. The latter allows for the incorporation of empirical data which can introduce viscous (Reynolds number) effects and Mach number effects at the rotor, if desired. The current analysis presented below does not include the effect of the wing on the rotor. Clark [8], using a panel method applied to the tilt rotor configuration, showed that although the local effects of the wing on the rotor are significant, the global effects on total torque and power are surprisingly small due to counterbalancing local effects.

The analysis below is used to independently obtain the pressure rise through the rotor disk and the swirl velocity immediately downstream of the disk. These are then used as boundary conditions for the Navier-Stokes code.

4.3.2 Combined Momentum Conservation - Blade Element Analysis

Glauert [39], McCormick [40], and Prouty [41] provide good discussions on momentum conservation and blade element analysis applied to propellers and/or rotors. The theory, as it is applied here, is outlined below.

The analysis assumes that (i) the slipstream produced by the rotor does not contract. This is a valid assumption for lightly or moderately loaded rotors, which is assumed to be the case here. (ii) There is no radial interference, i.e. the flow is two-dimensional at every spanwise station of the rotor. This assumption is valid except for a very small region near the blade tip. Small empirical corrections can be made for this effect, if desired. (iii) The torque and axial loads produced by the blade elements of the finite number of blades at distance r from the rotation axis, are averaged over the entire annulus. (iv) The rotation axis is aligned with the freestream u_∞ flow. We assume here, for convenience, that the propeller/rotor axis is horizontal. (v) The flow is incompressible.

Expression for the Thrust

Applying momentum conservation to an annulus of a cylindrical control volume at radius r, having width dr, and which extends to infinity upstream and downstream of the rotor,

$$dT = \underbrace{\rho\,(2\pi r\,dr)\,(u_\infty + w_a)}_{mass\ flow} \quad \underbrace{(2w_a)}_{velocity\ change} \tag{4.2}$$

where dT is the average elemental thrust force in the axial direction on an annulus of area $2\pi r\,dr$, u_∞ is the freestream velocity, w_a is the induced axial velocity in the rotor disk, and $2w_a$ is the induced axial velocity far downstream. Eq. 4.2 equates the net axial force with the rate of change of momentum (the mass flow multiplied by the net change in axial velocity).

That the induced axial velocity far downstream is twice that at the rotor plane

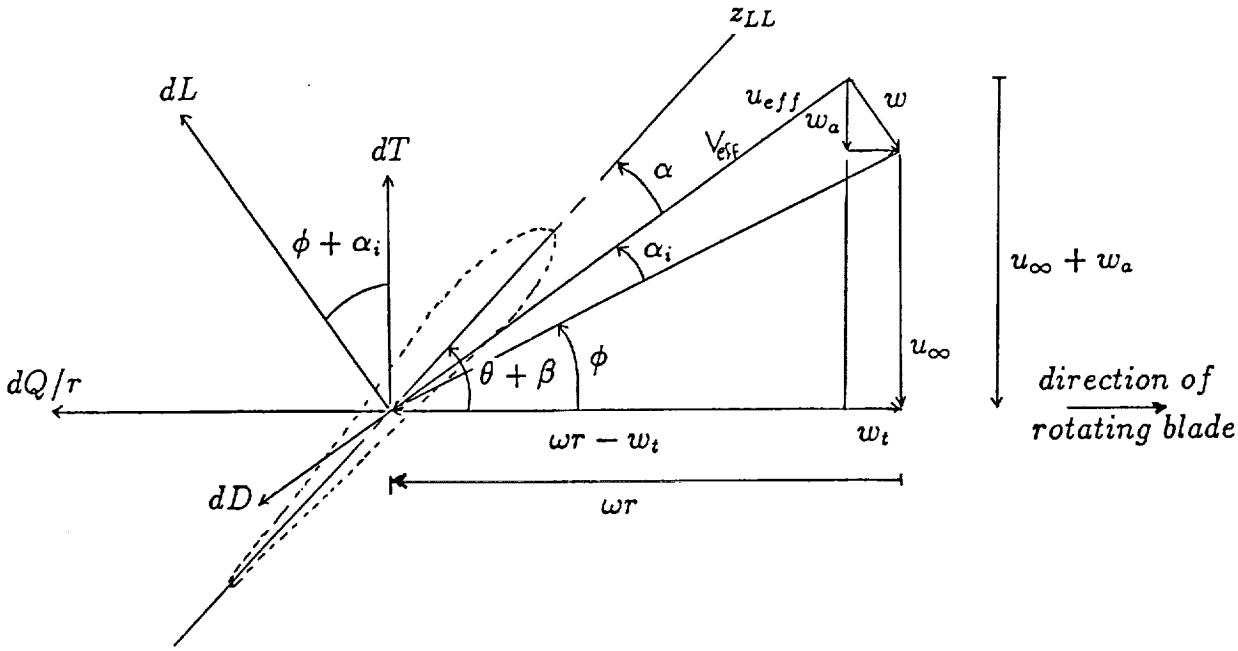

Figure 4.1: Relative velocity and force diagram at a rotor blade element.

can be shown in two ways. (i) Simple actuator disk theory using the principles of mass continuity and momentum conservation, and applying the Bernoulli equation twice – once upstream of the rotor disk, and once downstream of the rotor disk. (ii) Model the circulation on the rotor blade and the vorticity shed into the wake by horseshoe vorticies placed at each blade element.

The elemental thrust force can also be expressed in terms of the 2-D lift and drag of the airfoil at a blade element. Referring to the relative velocity and the force diagram of Figure 4.1, it can be seen that

$$dT = B\left(dL\cos\left(\phi + \alpha_i\right) - dD\sin\left(\phi + \alpha_i\right)\right) \tag{4.3}$$

where the total element thrust dT is equal to the sum of the contributions of all blades, B is the total number of blades, α_i is the induced angle of incidence, and ϕ is defined in Figure 4.1.

From the definition of the aerodynamic force coefficients,

$$dL = \frac{1}{2}\rho u_{eff}^2 C_l\, c\, dr$$

$$dD = \frac{1}{2}\rho u_{eff}^2 C_d c\, dr \tag{4.4}$$

where C_l and C_d are the two-dimensional airfoil lift and drag coefficients, respectively, c is the local blade chord, and u_{eff} is the effective velocity that the blade element sees.

Substituting Eqs. 4.4 into Eq. 4.3 ,

$$dT = \frac{1}{2}\rho u_{eff}^2 B\, c\, dr\, (C_l \cos(\phi + \alpha_i) - C_d \sin(\phi + \alpha_i)) \tag{4.5}$$

Equating Eqs. 4.2 and 4.5, and observing from Figure 4.1 that

$$(u_\infty + w_a)^2 = u_{eff}^2 \sin^2(\phi + \alpha_i)$$

we get:

$$\frac{w_a}{u_\infty + w_a} = \frac{Bc}{8\pi r} \frac{(C_l \cos(\phi + \alpha_i) - C_d \sin(\phi + \alpha_i))}{\sin^2(\phi + \alpha_i)} \tag{4.6}$$

Note that the aerodynamic coefficients can be expressed as a function of angle of incidence, α, i.e.

$$C_l = f_1(\alpha)$$
$$C_d = f_2(\alpha)$$

where, from Figure 4.1,

$$\alpha = \beta + \theta - (\phi + \alpha_i) \tag{4.7}$$

where β is the blade pitch angle setting, and θ is the local blade twist angle relative to the twist at the 75% radial station.

Empirically-derived section lift and drag characteristics as a function of angle of incidence can therefore be used in this analysis, thereby improving the predicted results for the rotor, and at the same time reducing the computational effort that would otherwise be required to generate this data using a Navier-Stokes solver, for example.

Note that for hover, $u_\infty = 0$, and the left hand side of Eq. 4.6 becomes unity. The only unknown in this equation, then, is α_i. The angle ϕ is zero when $u_\infty = 0$ (see Figure 4.1).

Expression for the Torque

The swirl velocity, w_t, is zero ahead (upstream) of the rotor, w_t at the rotor, and a constant $2w_t$ from immediately downstream of the rotor face to infinity downstream, in the inviscid analysis employed here.

The conservation of angular momentum equates the net torque produced by an annular element of the rotor on the fluid, with the rate of change of angular momentum (the mass flow multiplied by the net circumferential change in velocity multiplied by the moment arm r).

$$dQ = \underbrace{\rho\,(2\pi r\,dr)\,(u_\infty + w_a)}_{mass\ flow} \quad \underbrace{(2w_t)}_{velocity\ change} \quad r \tag{4.8}$$

Similar to the thrust analysis, the elemental torque contribution averaged on an annulus of width dr located a distance r from the axis of rotation can be written in terms of the elemental lift and drag loads. Referring to Figure 4.1,

$$dQ = B\,(dL\sin(\phi + \alpha_i) + dD\cos(\phi + \alpha_i)\,)\,r \tag{4.9}$$

Substituting Eqs. 4.4 into Eq. 4.9 and equating to Eq. 4.8 yields, upon re-arrangement,

$$\frac{w_t}{u_\infty + w_a} = \frac{Bc}{8\pi r}\frac{(C_l\sin(\phi + \alpha_i) + C_d\cos(\phi + \alpha_i)\,)}{\sin^2(\phi + \alpha_i)} \tag{4.10}$$

In hover, when $u_\infty = 0$, the left hand side of Eq. 4.10 reduces to w_t/w_a. Since α_i is determined from Eq. 4.6, then Eq. 4.10 can be solved for w_t/w_a.

Calculation of Required Quantities

Referring to Figure 4.1, it can be seen that

$$w = \sqrt{(u_\infty + w_a)^2 + (\omega r - w_t)^2}\ \sin\alpha_i\ =\ \sqrt{w_a^2 + w_t^2}$$

where ω is the angular frequency of rotation of the rotor. Re-arranging and setting $u_\infty = 0$ for hover, we get for the local induced axial velocity

$$w_a = \frac{\omega r}{\frac{\sqrt{\cos^2 \alpha_i + (w_t/w_a)^2}}{\sin \alpha_i} + (w_t/w_a)} \tag{4.11}$$

Once w_a is calculated using Eq. 4.11 knowing w_t/w_a from Eq. 4.10, then the swirl velocity w_t is immediately known as well.

Applying the Bernoulli equation upstream of the rotor and again downstream of the rotor, we find that the pressure rise across the rotor, Δp, in hover, is

$$\Delta p = 2\rho w_a^2$$

The total thrust and torque on the rotor disk is calculated by integrating the radial thrust gradient and radial torque gradient, respectively. Eqs. 4.2 and 4.8 can be easily written in terms of dT/dr and dQ/dr, respectively. Then

$$\begin{aligned} T_{TOT} &= \int_0^R (dT/dr)\, dr \\ Q_{TOT} &= \int_0^R (dQ/dr)\, dr \end{aligned}$$

The total thrust coefficient and total torque coefficient are calculated using the standard definitions:

$$\begin{aligned} C_T &= \frac{T_{TOT}}{\rho A \left(u_\infty^2 + (\omega R)^2\right)} \\ C_Q &= \frac{Q_{TOT}}{\rho A \left(u_\infty^2 + (\omega R)^2\right) R} \end{aligned}$$

where A is the rotor disk area and R is the blade radius.

Solution Procedure

For a given rotor having specified blade geometry and for a given thrust coefficient, C_T, an iterative solution procedure outlined below gives the radial distributions of axial and swirl velocities and pressure rise, at a converged value of blade pitch angle setting, β.

1. Input rotor RPM, and rotor geometry including:

   - number of blades
   - rotor radius
   - blade planform shape, i.e. local chord, c, distribution
   - blade twist relative to the 75% radial location

2. Input 2-D airfoil characteristics: C_l, C_d vs. α.

3. Input desired total thrust coefficient, C_T.

4. Make an initial guess for the blade pitch angle, β.

5. Divide the rotor disk into a number of annular rings. At each, calculate the induced angle of incidence, α_i, using Eq. 4.6. Calculate the effective angle of incidence, α, from Eq. 4.7. Use the inputted 2-D airfoil data to determine the C_l and C_d corresponding to α.

6. Calculate w_a, w_t, Δp, dT/dr, and dQ/dr at each annulus.

7. Integrate along the radius to obtain C_T and C_Q.

8. If C_T is within a certain specified tolerance from the desired, inputted value of C_T, then the solution is converged; otherwise, go to (4) and repeat steps (4) through (8).

Figure 4.2 is an example of the output generated from this analysis, for a 3-bladed, 7-ft diameter rotor similar to the 0.16 scale model tested at the NASA Ames Outdoor Aerodynamic Research Facility. For this example, NACA 0012 airfoil data was substituted for the aerodynamic characteristics of the actual rotor blade sections.

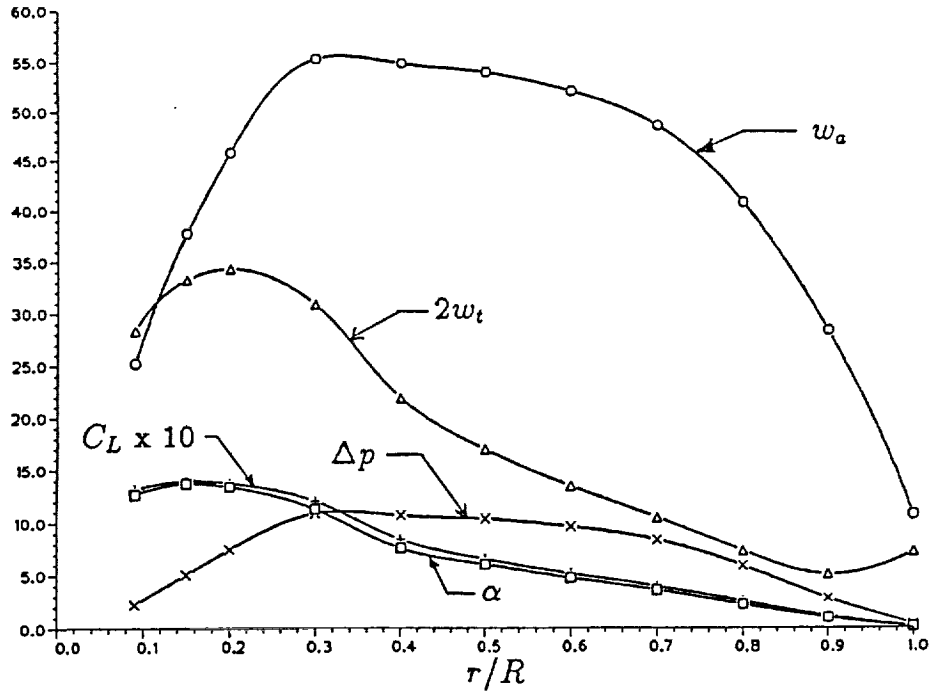

Figure 4.2: Sample output from the momentum theory/blade element analysis for a 7-ft diameter, 3-bladed rotor at 2090 RPM and with $C_T = 0.0065$.

4.3.3 Grid Used for Modeling the Rotor

To limit the size of the computational domain, it was originally intended to extend the inflow boundary only to the horizontal plane containing the rotor. Solution convergence problems were encountered, however, due to the close proximity of the boundary to the wing whose presence induces large flow gradients near the inflow plane. It was decided, therefore, to increase the size of the physical domain so as to include the effect of the large-scale entrainment of flow back into the top of the rotor. An inner zone surrounding the wing and extending to the rotor plane was developed. An outer zone was also created which encircled the inner grid and extended approximately 20 rotor diameters from the wing in all directions. The outer grid line of the inner zone matches exactly the inner grid line of the outer zone. See, for example, Figures 5.20 and 5.21. Consecutive, independent solutions are performed on the inner and outer zones until adequate convergence is achieved.

Everywhere along this common boundary between the two zones except for points

located in the region defined by the rotor disk, simple averaging of the flow properties is performed to couple the two solutions. For a given spanwise grid station, k, and a given chordwise index, j, the most recently computed values of the flow properties at the interior grid points immediately to either side of the common boundary are averaged. This same procedure is applied both for the outer boundary points of the inner grid and the inner boundary points of the outer grid. This averaging assures a continuity of mass across the common boundary.

The outer boundary grid points of the inner zone that lie within the rotor disk are viewed as an inflow boundary. From a method of characteristics analysis, as discussed in Section 4.2, a subsonic inflow boundary requires specification of four quantities and extrapolation of the fifth. The interior values of ρu, ρv, and ρw are averaged across the disk as described above, and these averages used as inflow boundary conditions for the inner zone. The pressure, p, is obtained from the pressure at the first interior point of the outer zone (just above the rotor face). To this is added the pressure rise, Δp, obtained in the momentum conservation theory/blade element analysis of Section 4.3.2 . The density, ρ, is extrapolated from the interior of the inner zone using zero-order extrapolation. To include the effects of swirl, the tangential velocity, w_t, obtained from the analysis of Section 4.3.2, can be decomposed into a u and v contribution in the horizontal plane and used to replace the values above obtained by averaging.

For the inner boundary grid points of the outer zone that lie within the rotor disk, search for the best combination of boundary conditions is still being pursued. Currently, averaging across the rotor is used to specify the boundary conditions for all the flow variables but the pressure. For the pressure, the prescribed pressure rise, Δp, is subtracted from the most recently-computed value of p at the nearest interior point in the inner zone. Specifying Δp across a zonal boundary was first suggested to the authors by Tavella [42].

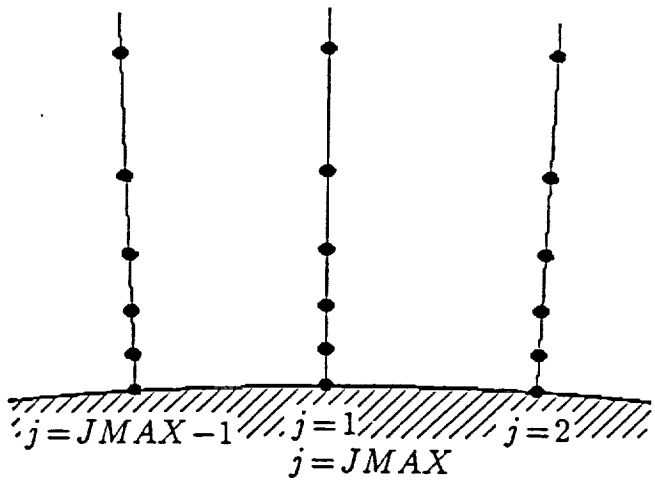

Figure 4.3: One-point overlap grid for wall jet boundary conditions.

4.4 Wall Jet

In previous CFD studies (for example, reference [19]), multiple zones were used to model a tangential, circulation control jet on the surface of an airfoil. Preliminary calculations during the course of the current research, however, have demonstrated that a single-zone grid, an approach suggested by Tavella [42], is suitable for this computation.

The grid must have sufficient grid density in the jet region to resolve the jet flow and associated entrainment of the outer flow. For easier implementation of boundary conditions for the wall jet, the 3-point grid overlap in the chordwise j index normally used, is reduced to a 1-point overlap (see Figure 4.3).

The wall jet boundary conditions are specified on the $j = JMAX$ line. The grid is defined such that 10 - 20 grid points lie within the $\approx 0.1\%$ chord jet slot height. Beyond this jet region, the values of the flow properties at $j = 1$ and $j = JMAX$ are obtained by taking the average of the values at the corresponding interior points at $j = 2$ and $j = JMAX-1$. Within the slot region, the $j = JMAX$ grid points are viewed as an inflow boundary. A total pressure corresponding to the plenum pressure used in the model tests, a total temperature assumed to be freestream ambient, and jet

exit angle are all specified. The jet is assumed to be tangent to the airfoil surface at the jet exit. The magnitude of the jet exit velocity is calculated assuming isentropic expansion of the compressed air from the plenum to local static pressure at the jet exit . The $j=1$ grid points that overlap the $j=JMAX$ points in the jet are viewed as outflow boundary points. Pressure is specified and set equal to that at the jet exit. Zero-order extrapolation from the $j=JMAX-1$ values is used for all the other flow properties.

4.5 Initial Conditions

The steady-state (or pseudo steady-state in this case where some residual unsteadiness due to vortex shedding off the wing leading and trailing edge may exist) solution of a hyperbolic system of partial differential equations is independent of the initial conditions. In our case, the interior points can be seeded initially with a freestream flow close in magnitude to the expected rotor slipstream velocity, or the interior could be set initially to have zero flow everywhere. Both of the above initial conditions yield the same final results, with similar rates of convergence.

Chapter 5

Discussion of Results

5.1 Preliminary Comments

The computation of tilt rotor flowfields using the Navier-Stokes equations is a challenging task. A problem such as this is best divided into smaller, more manageable parts, and a step-by-step approach used to reach the final objective. That is why this preliminary CFD study of tilt rotor flowfields has focused on the calculation of subsets of this complicated 3-D flow.

In the following discussion, freestream results both in 2-D and in 3-D are presented for an airfoil and a wing, respectively, at an angle of incidence of -90 degrees. The rotor alone was modeled as an actuator "line" in 2-D and as an actuator disk in 3-D with and without swirl. These results are followed by two-dimensional wing/rotor interaction computations. Preliminary results for 3-D wing/rotor interaction are also discussed. Finally, the results of a 2-D tangential blowing calculation are presented. These computations serve as building blocks necessary to ensure the successful completion of the final objective – to compute accurately the three-dimensional tilt rotor flowfield with a wing having tangential blowing for leading edge separation control.

All plots shown in this chapter were generated using PLOT3D, an interactive graphics package developed at NASA Ames Research Center [43,44].

5.2 Freestream Calculations (No Rotor)

5.2.1 Results in Two Dimensions

Figure 5.1 shows two views of a typical grid used to calculate the freestream flow around the V-22 airfoil section at an angle of incidence of -90 degrees. In order to resolve the fine details of the flow in the region of a blunt trailing edge, very high grid resolution is required. The focus of this work was not on the trailing edge flow alone. For this reason, as is often done in CFD airfoil work, the original trailing edge is extended to a point and the modified airfoil is re-scaled to the original chord length. The V-22 airfoil trailing edge thickness is considerably less than 0.5% chord so the modification to the airfoil section is slight. A 2-D elliptic grid solver is used to obtain a smooth distribution of grid points. Exponential clustering produces a fine mesh near the airfoil surface. As discussed in Section 4.2, five identical, parallel 2-D grid planes are required for the two-dimensional calculations so as to accommodate the 5-point, fourth-order differencing stencil used on the right hand side of Eq. 2.23. Symmetry boundary conditions are imposed on both ends of the grid, to simulate an infinitely-high aspect ratio wing.

Figures 5.2 to 5.5 are all results of a "pseudo" 2-D calculation. A freestream flow of $M = 0.2$ at $\alpha = -90°$ is imposed on the upper inflow boundary. A Reynolds number of 0.5 x 10^6 is selected as being representative of the small scale (≈ 0.16 scale) model flow in tests that were – and that will be – undertaken at NASA Ames' Outdoor Aerodynamic Research Facility (OARF) – refer to Section 1.2.1. A time-accurate computation is performed, i.e. the time step is sufficiently small to resolve the unsteadiness in the flow.

Figure 5.2 shows the velocity vectors around the airfoil at two different points in time. In the upper picture, a vortex has just been shed off the airfoil leading edge. In the lower picture, a vortex has just been shed off the trailing edge. This

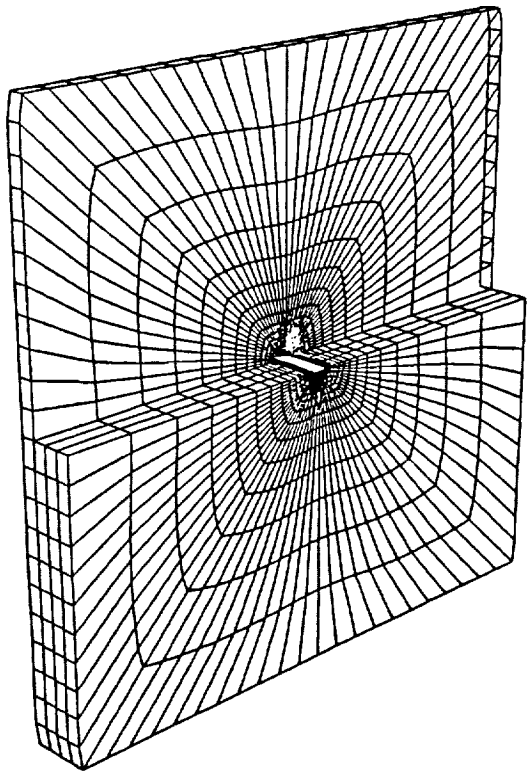

(a) Cutaway, farfield view of the grid.

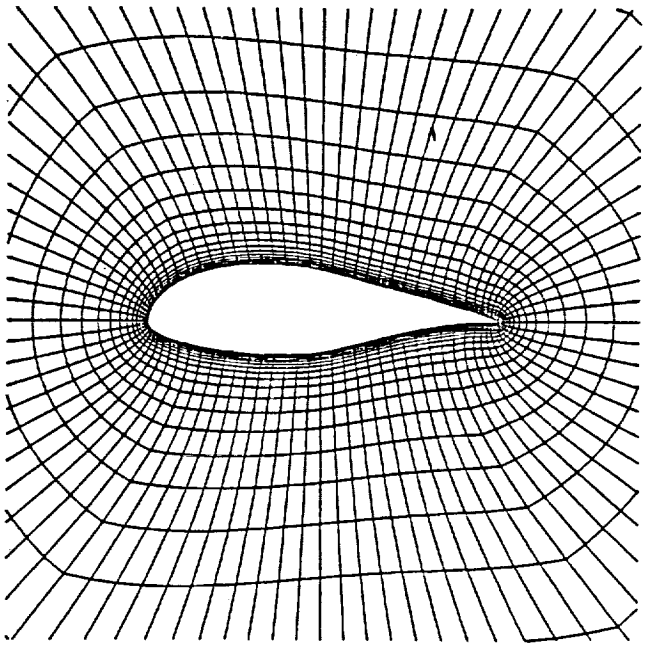

(b) Close-up view of the airfoil gridding.

Figure 5.1: Views of a 2-D O-grid around the V-22 airfoil.

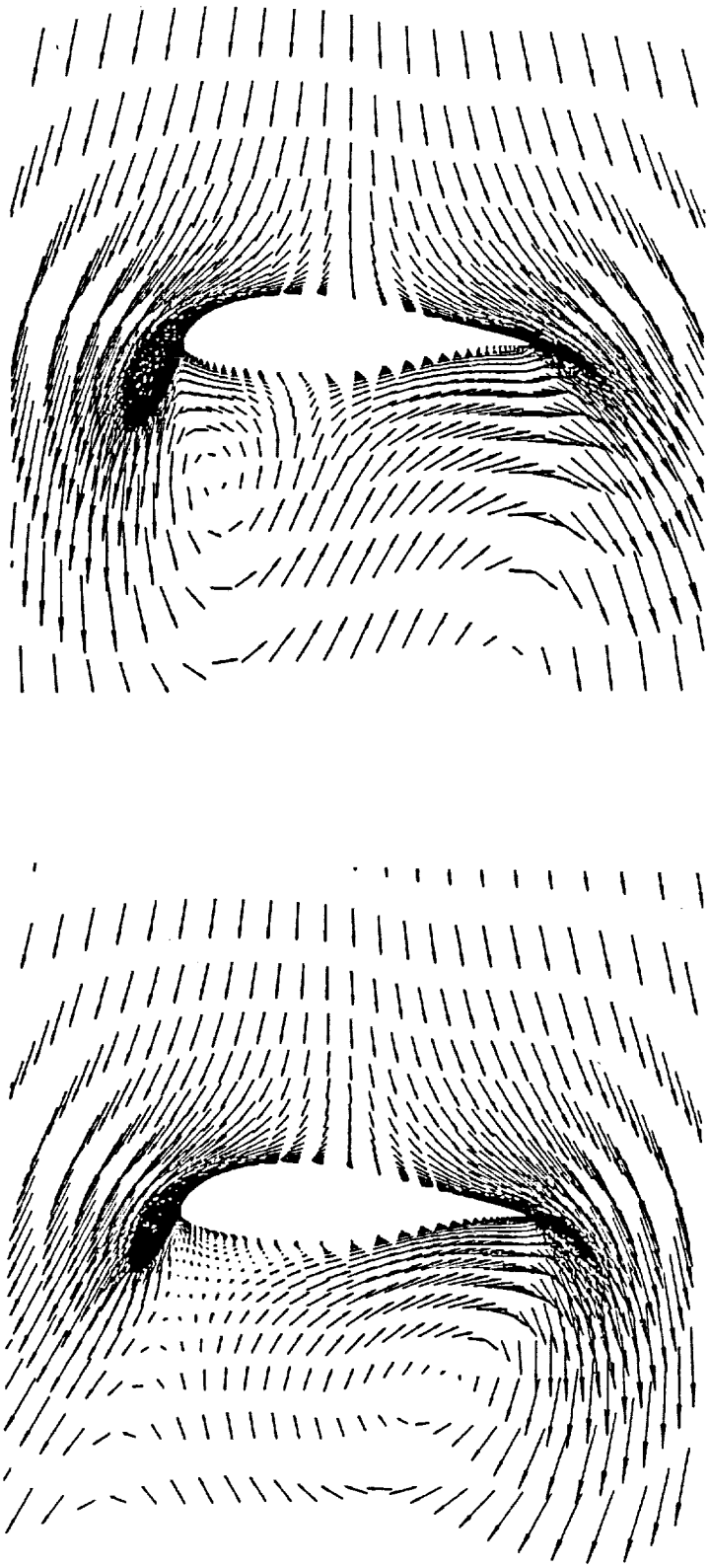

Figure 5.2: Velocity vector plots about the V-22 airfoil at two different points in time, in a $M_\infty = 0.2, \alpha = -90°$ flow.

asymmetric vortex shedding is typical of the vortex streets created behind bluff bodies at these Reynolds numbers. The frequency of this shedding was computed to be about 16 cycles per second. For comparison purposes, a 2-D cylinder, at the same Reynolds number, whose diameter is equal to the airfoil chord, typically produces vortex shedding at the rate of about 30 cycles per second. This value was obtained from an empirical relation in reference [45]:

$$\frac{fd}{u_\infty} = 0.198\left(1 - \frac{19.7}{Re}\right)$$

where f is the frequency of vortex shedding and d is the cylinder diameter which, for the above calculation, was set to 0.447 meter which is the 0.16 scale model wing chord. No experimental data exists for the V-22 airfoil to confirm the accuracy of this unsteady, computational result. Examining the velocity profile at the airfoil surface, it can be observed that the boundary layer has been resolved. Figure 5.3 is a close-up view of the flow around the wing leading edge. Separation is seen to occur at a location on the airfoil upper surface slightly aft of the leading edge. This, of course, changes somewhat with time due to the unsteady nature of this 2-D flow. Note that in this and all subsequent calculations discussed in this report, laminar flow was assumed – i.e. no model has as yet been implemented to model turbulence effects.

Figure 5.4 is a Mach contour plot of the flowfield at one point in time. Note that the flow stagnates in the mid-chord region on the upper surface, and beyond the leading and trailing edges, the flow accelerates to about $M = 0.26$.

A computation was performed where large time steps were taken to accelerate convergence to a "pseudo" steady-state solution. The resulting pressure distribution is shown in Figure 5.5. The general shape of the C_p distribution compares favorably with the download distribution of Figure 1.3. The loop in the distributions near the leading edge indicates a deceleration of the flow even before it gets to the leading edge. This was observed previously in Figure 5.3. The base pressure is fairly uniform along

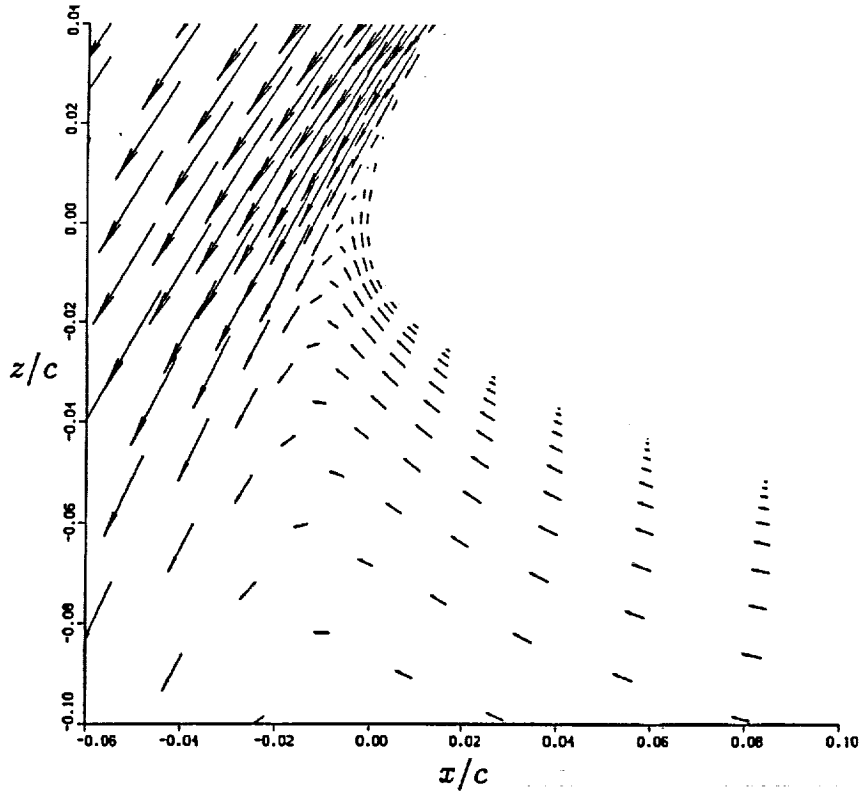

Figure 5.3: Close-up view of the velocity vectors around the V-22 airfoil leading edge, in a $M_\infty = 0.2, \alpha = -90°$ flow.

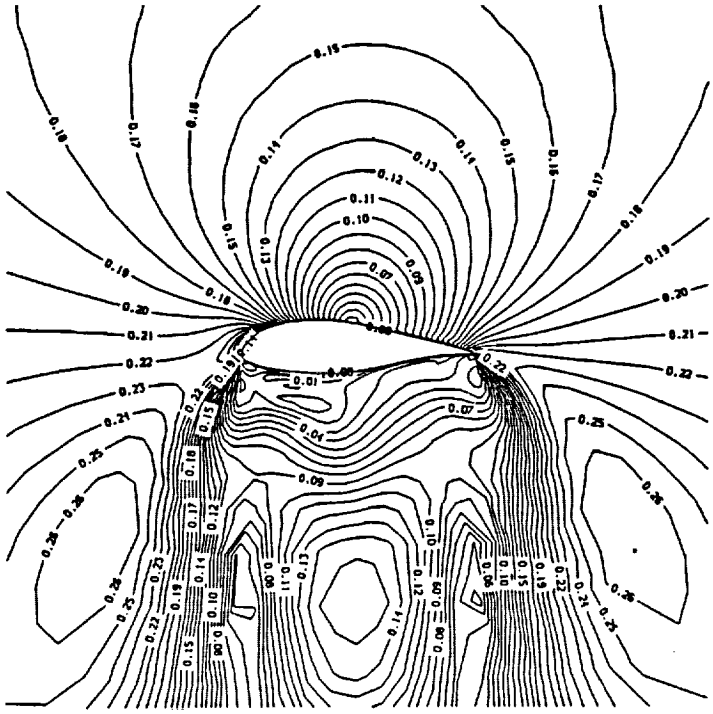

Figure 5.4: Mach number contours about the V-22 airfoil, in a $M_\infty = 0.2, \alpha = -90°$ flow.

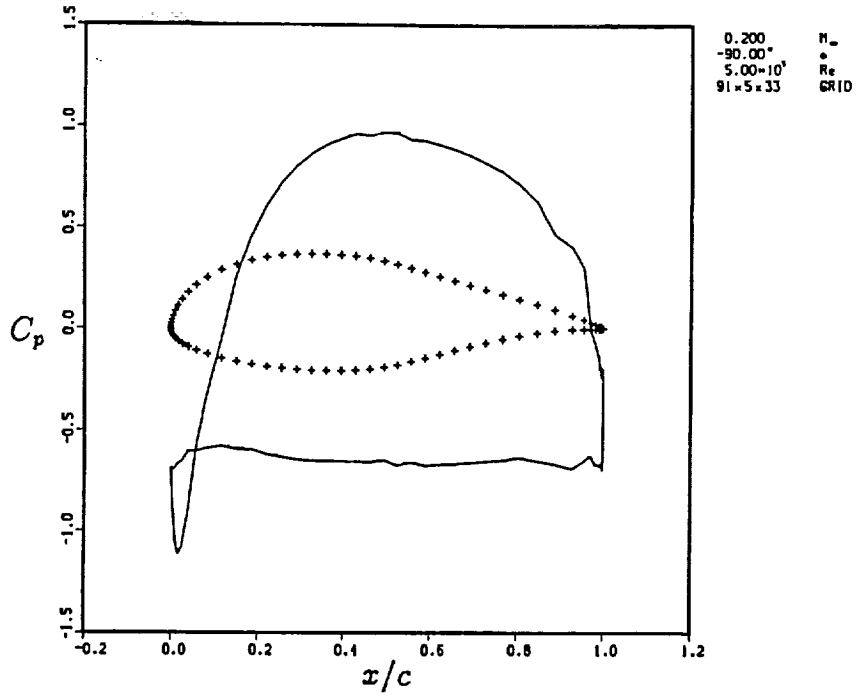

Figure 5.5: Surface pressure coefficient distribution on the V-22 airfoil, in a $M_\infty = 0.2, \alpha = -90°$ flow.

the airfoil lower surface; this is also seen experimentally. The computed base pressure is higher than wind tunnel measurements. This is most likely due to the inaccuracy of the steady-state calculation for time dependent problems. The computed flowfield below the airfoil showed two symmetric vortices of equal strength but opposite sense of rotation whose centers were located over a chord length downstream of the airfoil. Certainly, in the future, it would be better to run the code in a time accurate fashion and take a time average of the desired flow characteristics. A pressure integration around the airfoil yields a computed 2-D drag coefficient C_d of 1.2. This compares to $C_d \approx 1.6$ obtained from wind tunnel tests of the XV-15 airfoil [6].

5.2.2 Results in Three Dimensions

As discussed in Section 3.1, a grid for three-dimensional calculations is generated by placing a series of 2-D grids at various spanwise stations along the wing and beyond the wing tip. Exponential stretching increases the grid density near the tip where the

three-dimensional effects are most significant. The wing is based on the dimensions of the 0.16 scale model used in the NASA Ames OARF tests. It has an aspect ratio of 6.1 and is of constant chord with no twist or sweep. By comparison, the V-22 wing has an aspect ratio of 5.5 and 6° of forward sweep. The outer boundary of the grid extends 20 chord lengths in all directions. As mentioned previously, due to symmetry of the flow about the centerline, only one half of the wing needs to be modeled. For the results shown in this section, the grid has 47 points defining the wing surface. Each grid line extending from the body to the outer boundary is defined using 33 points, with exponential clustering near the surface. There are 35 parallel 2-D grid planes defining the spanwise grid distribution. This yields just over 54,000 points in total. A converged solution takes about 700 time steps and about 30 minutes of CPU time on the Cray-XMP supercomputer. Figure 5.6 shows two views of the grid employed. Figure 5.6(a) is a cutaway perspective view of the grid, and Figure 5.6(b) is a horizontal cut through the wing chord $(x - y)$ plane and including the upper surface gridding. The wing tip is defined arbitrarily to be the last 5% of the wing semi-span, and it has a chord variation that is elliptic, with each tip airfoil section having the same thickness-to-chord ratio, t/c. It can be seen from Figure 5.6(b) that the tip region is not well-defined, and the mesh is highly skewed here. Improvements in gridding the tip region will be pursued in future work.

Figures 5.7 and 5.8 are both views of the flow features in a vertical plane running spanwise through the wing mid-chord. Figure 5.7 is a plot of velocity vectors for a freestream flow of $M = 0.2$ at $\alpha = -90°$, the same as for the 2-D case. Figure 5.8 shows the corresponding Mach number contours. Both of these plots show that much of the span of the wing in the mid-chord region sees stagnated flow. The flow becomes increasingly more spanwise as the tip is approached, as expected. The flow accelerates around the tip, and viscous effects give rise to a very pronounced vortex beneath the tip.

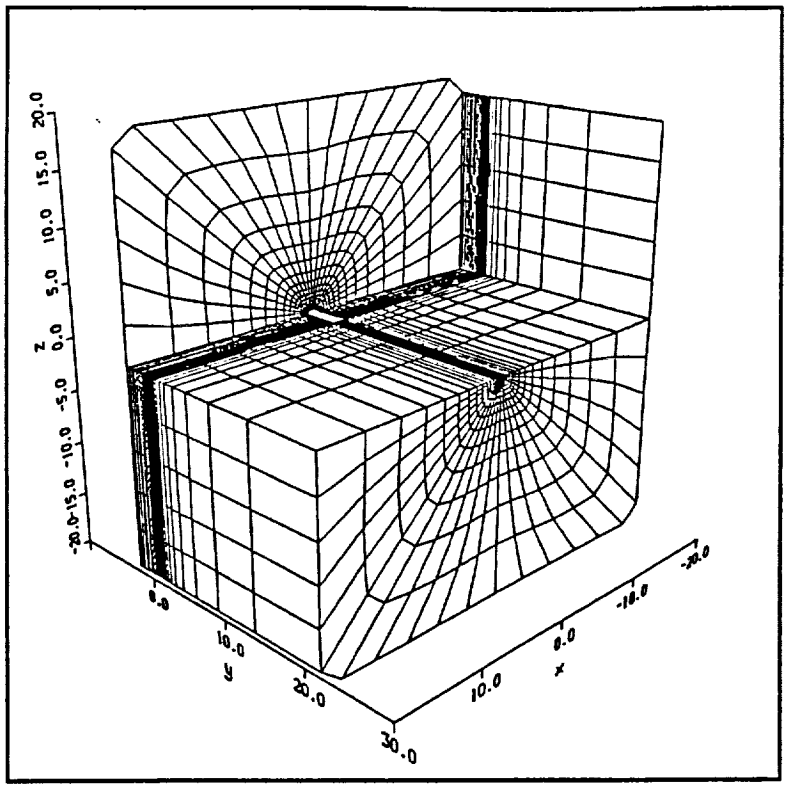

(a) Cutaway view of the grid.

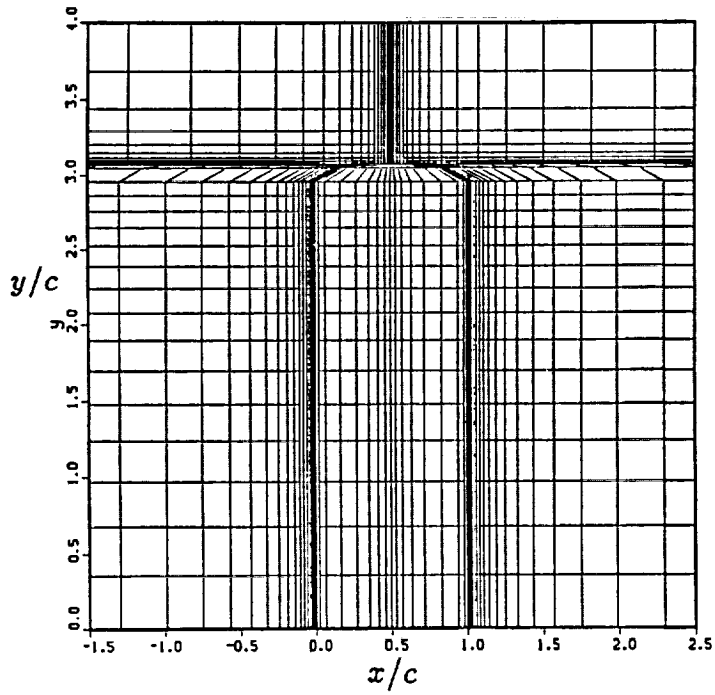

(b) An $x - y$ cut through the wing chord plane and including the wing upper surface grid distribution.

Figure 5.6: Views of a 3-D grid around the finite-span wing.

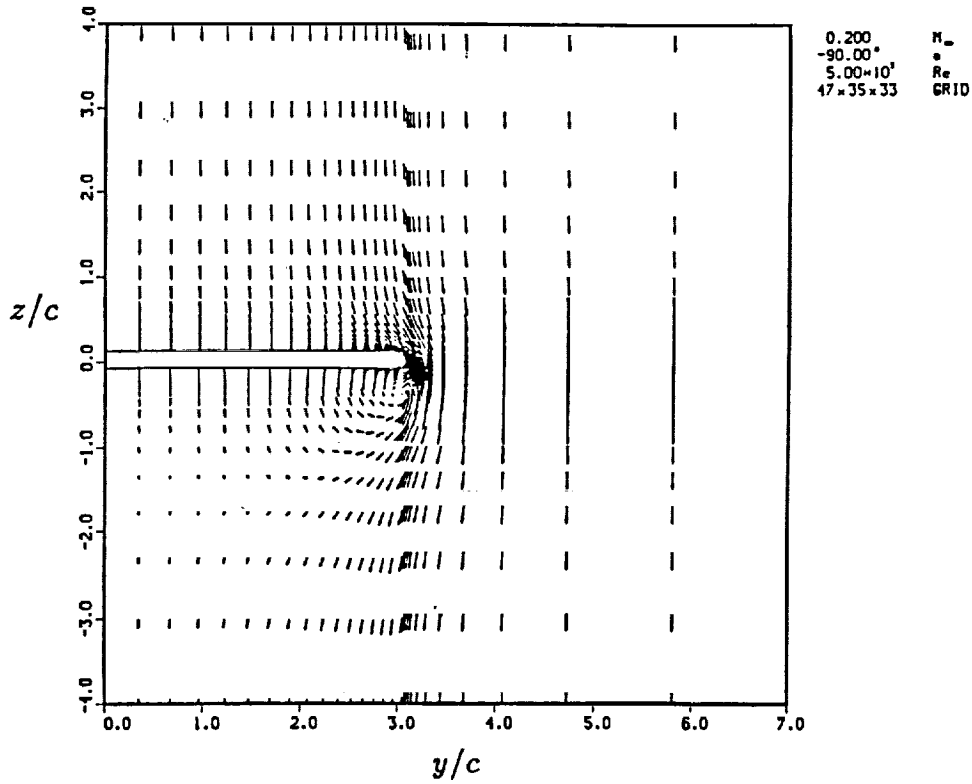

Figure 5.7: Velocity vectors in a vertical plane running spanwise through the wing mid-chord, in a $M_\infty = 0.2, \alpha = -90°$ flow.

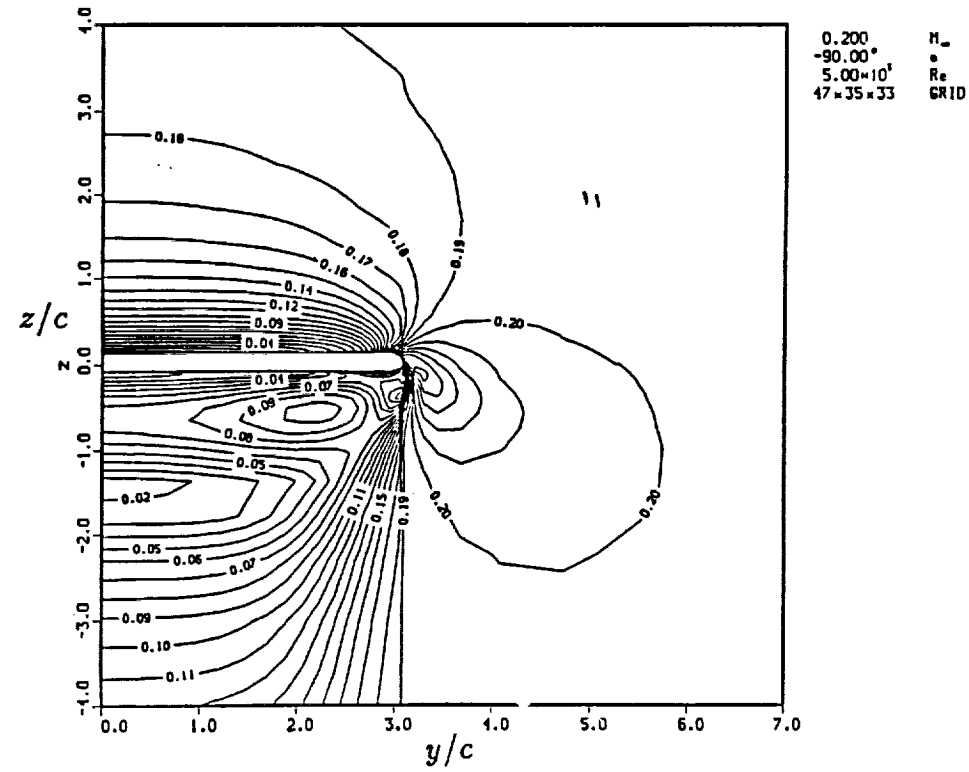

Figure 5.8: Mach number contours in a vertical plane running spanwise through the wing mid-chord, in a $M_\infty = 0.2, \alpha = -90°$ flow.

Figure 5.9 is a view of the velocity vectors above the wing surface and in the $x-y$ plane beyond the wing. The stagnation region runs from the centerline to about half

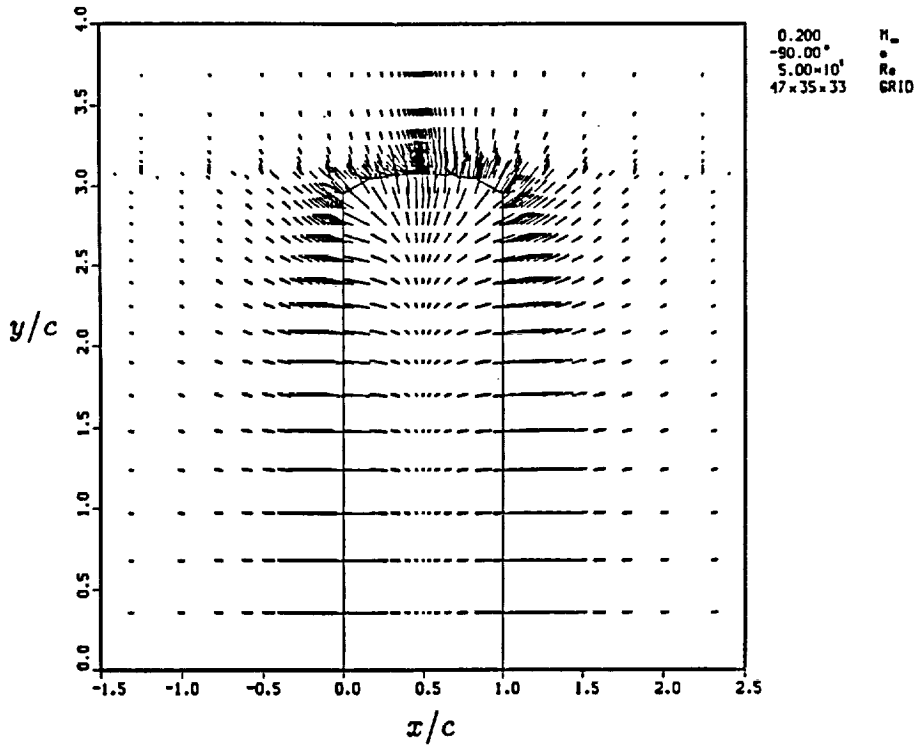

Figure 5.9: Velocity vectors just above the wing and beyond the wing in the $x-y$ plane, in a $M_\infty = 0.2, \alpha = -90°$ flow.

way to the wing tip. In this region, the flow is primarily two-dimensional in character. From the mid-span region outboard to the tip, the flow becomes increasingly spanwise before rounding the tip where it is rapidly re-directed by the freestream.

Figure 5.10 shows five separate chordwise surface pressure coefficient distributions, each at a different spanwise location on the wing. Three-dimensionality is again observed in the form of changing pressure distributions particularly in the tip region. For all spanwise stations, the wing leading edge induces a greater flow acceleration than the trailing edge - as evidenced in lower peak C_p's at the leading edge.

Figure 5.11 shows seven separate upper surface pressure coefficient distributions, each for a different percent chord location. Here, tip effects are clearly shown. The

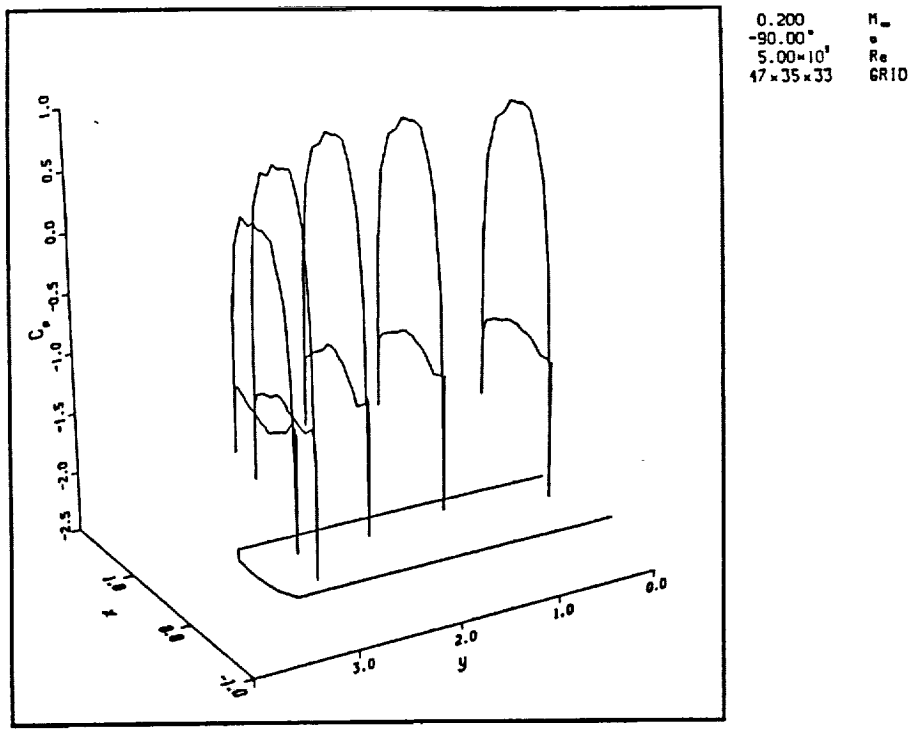

Figure 5.10: Typical chordwise surface pressure coefficient distributions at various spanwise stations along the wing, in a $M_\infty = 0.2, \alpha = -90°$ flow.

pressure coefficient for all but the leading edge C_p distribution drops sharply at the tip. Kinks in the tip region are due to insufficient grid-point density. Along the wing leading edge, as the tip is approached from the mid semi-span, the flow is accelerated not only by the 2-D flow effect around the leading edge, but also by the increasing, 3-D spanwise flow. That is why the negative pressure coefficient starts to increase well inboard of the tip. After a certain point, as evidenced by the peak in the leading edge C_p distribution, the spanwise flow dominates and the flow acceleration diminishes because less of the flow travels around the leading edge to the lower surface.

5.3 Rotor Alone in Two and Three Dimensions

Initially the inflow boundary (upper boundary - see, for example, Figure 5.6) for the wing/rotor computation was to be the plane of the rotor. The rotor was to

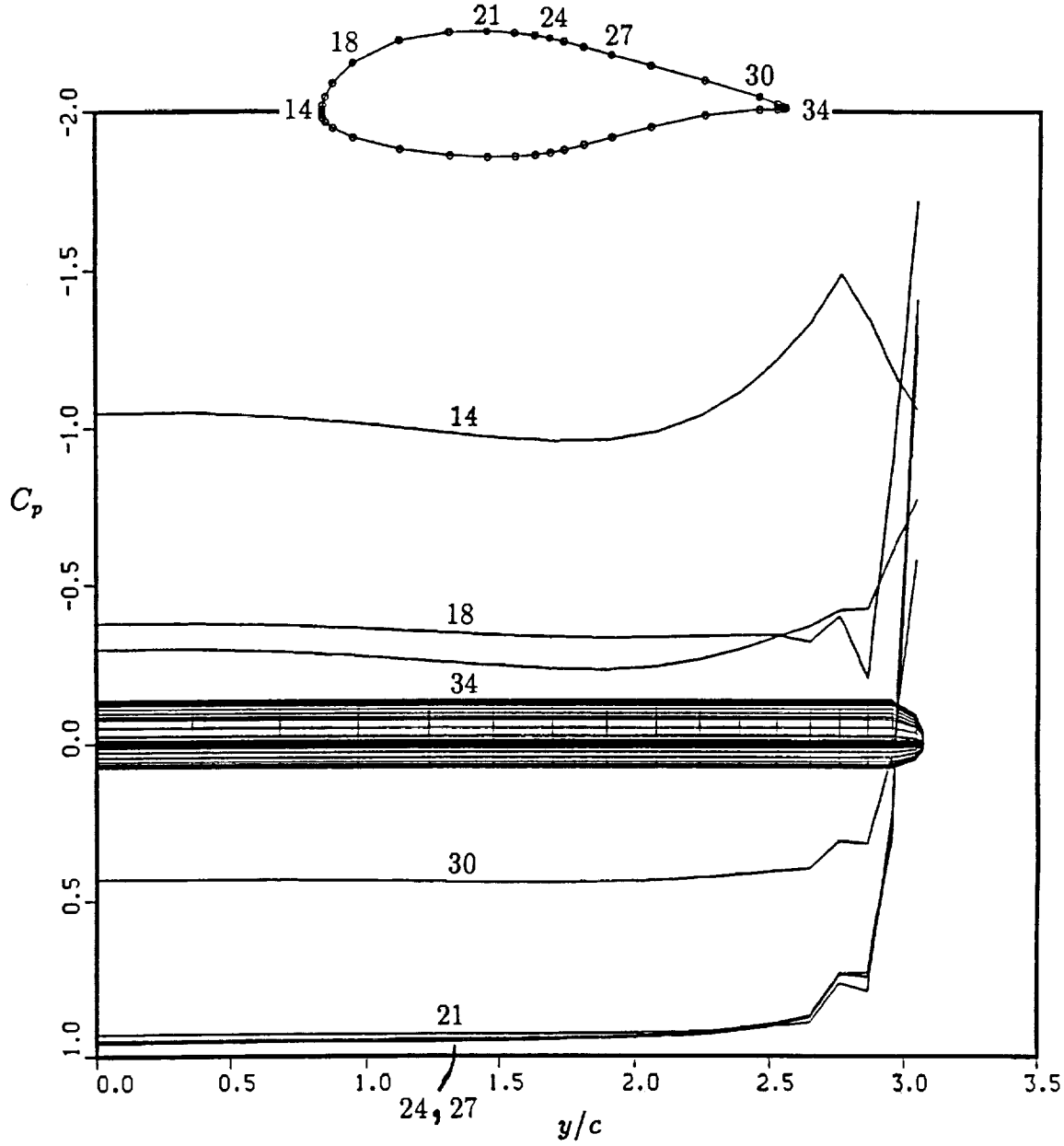

Figure 5.11: Spanwise upper surface pressure coefficient distributions at seven different chordwise locations along the wing, in a $M_\infty = 0.2, \alpha = -90°$ flow.

be modeled by specifying a pressure and velocities corresponding to a lifting rotor (obtained from the momentum theory/blade element analysis of Section 4.3). It is unclear, however, what boundary conditions to impose at those grid points that are on the inflow boundary but away from the rotor disk. Being an inflow boundary, pressure and velocity should be specified, for consistency. These, however, are not known to sufficient accuracy. A previously-developed vortex panel model of the tilt rotor was deemed inadequate to provide this information. Additionally, no velocity or pressure surveys have been performed that could be of assistance. Computational results that were obtained by extrapolating values of the flow properties from the interior of the solution to the upper boundary were not satisfactory. Another drawback of this initial approach is the fact that because the pressures and velocities were specified at the rotor face, the influence of the wing was completely decoupled from the rotor.

For these reasons, it was decided to model the rotor using two zones, and a multiple zone algorithm. The common boundary between the two zones is selected to coincide with the location of the rotor. This allows specification of a pressure rise, Δp , across the disk without having to fix the static pressure itself. The pressure in the rotor plane, then, can float under the influence of the wing below. The use of two zones also extends the solution domain much further thereby permitting the resolution of the fountain flow and the large scale recirculation pattern through the rotor.

Figures 5.12 and 5.13 show the results of two different two-dimensional calculations using a Cartesian grid comprised of two zones, one above the other. Each zone has 47 grid lines in the direction parallel to the rotor axis of rotation and 17 grid lines perpendicular to the rotor axis. The common boundary between the zones is used to define the rotor boundary conditions. Exponential stretching is used to cluster the grid points in the location of the rotor. The freestream velocity was set to

$M_\infty = 0.001$ so the flow is driven exclusively by the specified pressure rise across the rotor. Here, the magnitude of the pressure rise, Δp, is 10% of freestream ambient pressure. The actuator "line" of these 2-D calculations is assumed to be uniformly loaded, i.e. Δp = constant.

Figure 5.12 shows the instantaneous particle traces (same as streamlines in steady flow) through the rotor disk. For inviscid flow, the flow accelerates through the

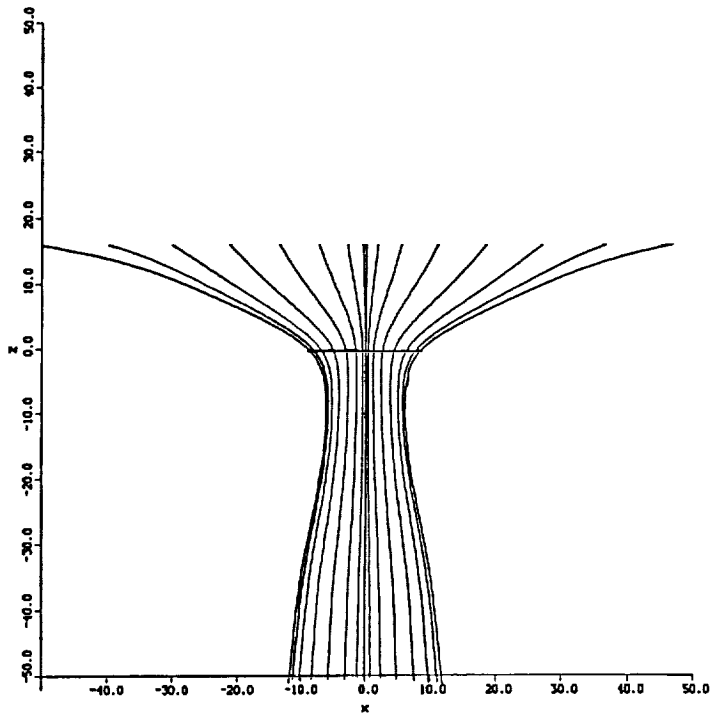

Figure 5.12: Particle traces released in a flow through a 2-D actuator disk, where $\Delta p = 0.01 p_\infty$.

rotor disk reaching a maximum velocity downstream of the disk. Theoretically, this flow momentum is maintained indefinitely. The slipstream, therefore, contracts to a minimum width below the rotor, and thereafter remains unchanged. Examining Figure 5.12, it is seen that the computed slipstream contracts to a minimum width, as expected, but then begins to expand slowly indicating that there is a corresponding deceleration of the flow. This behavior is unrelated to the contribution of the viscous terms in the Navier-Stokes equations because the same results are obtained for the

Euler equations alone. Admittedly, an actual rotor slipstream diffuses within a few rotor diameters. Since it is not the physics modeled by the equations that is causing the diffusion, it must, therefore, be due entirely to numerical dissipation. Numerical dissipation is caused by the truncation error associated with the spatial differencing of the partial differential equations. It increases with grid cell size. Mesh refinement, then, i.e. a finer mesh, would reduce the computed diffusion of the rotor slipstream.

Figure 5.13 shows the pressure above and below the rotor. As anticipated from

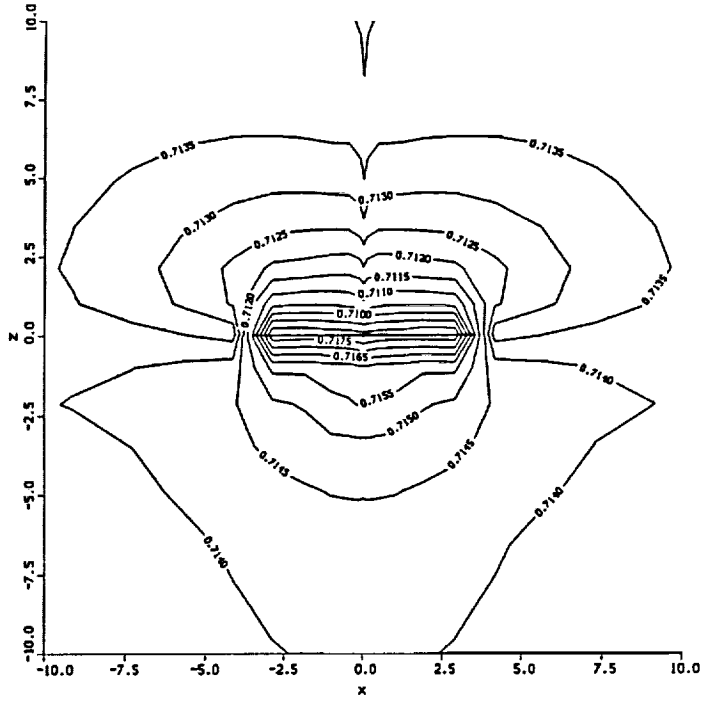

Figure 5.13: Pressure contours for a flow through a 2-D actuator disk, where $\Delta p = 0.01 p_\infty$.

simple momentum theory, the pressure far above the rotor is at freestream ambient (non-dimensionalized $p_\infty = 1/\gamma = 1/1.4 = 0.7143$). The static pressure drops to a minimum value just above the rotor due to the accelerating flow being drawn into the rotor disk. The rotor produces an increase in total pressure, which in this figure, is seen as a step in the static pressure immediately downstream of the rotor. The pressure then decays back towards its original freestream value as the flow accelerates

to a near constant value downstream of the rotor. As expected, the flow gradients increase as the rotor disk is approached.

Three-dimensional results are obtained for a rotor by creating a mesh in the form of a rectangular box. A horizontal plane through the middle of this grid forms the common boundary between the upper and lower zones. Each zone is comprised of 35 stacked, parallel 2-D grid planes. Each grid plane is identical to that used for the 2-D calculations discussed above.

Figures 5.14 – 5.19 are results from a computation where Δp across the rotor is set to a uniform $0.05p_\infty$, the freestream is essentially zero ($M_\infty = 0.001$), and the rotor diameter is 6 units. The plots focus on a small portion of the entire domain which extends to 100 units in all directions. Figure 5.14 shows the computed velocity field in the near vicinity of the lifting rotor on a vertical plane through the rotor axis. Note that far above the rotor, the flow velocity is near zero. The

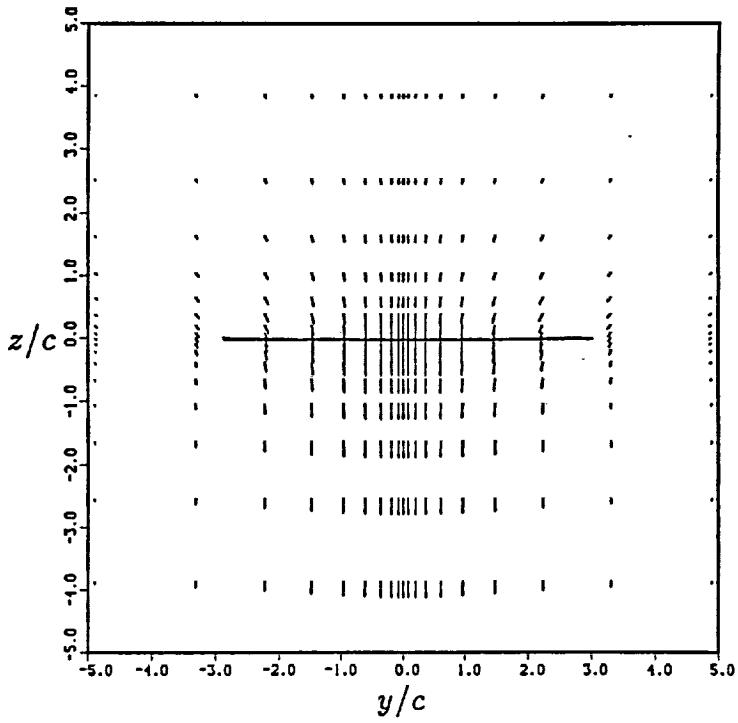

Figure 5.14: Velocity vectors in a vertical plane through the 3-D actuator disk, where $\Delta p = 0.05p_\infty$.

flow accelerates continuously down through the rotor until it reaches a maximum value within a rotor radius downstream of the rotor face. Simple, incompressible momentum considerations in 1-D indicate that the maximum axial velocity, induced by an actuator disk in zero freestream flow, is twice that of the velocity in the rotor plane. Qualitatively, this can be seen in the figure by comparing the velocity vector lengths in the rotor plane with those far downstream. Figure 5.15 shows the accompanying particle traces through the rotor disk. Figure 5.16 is a plot of the

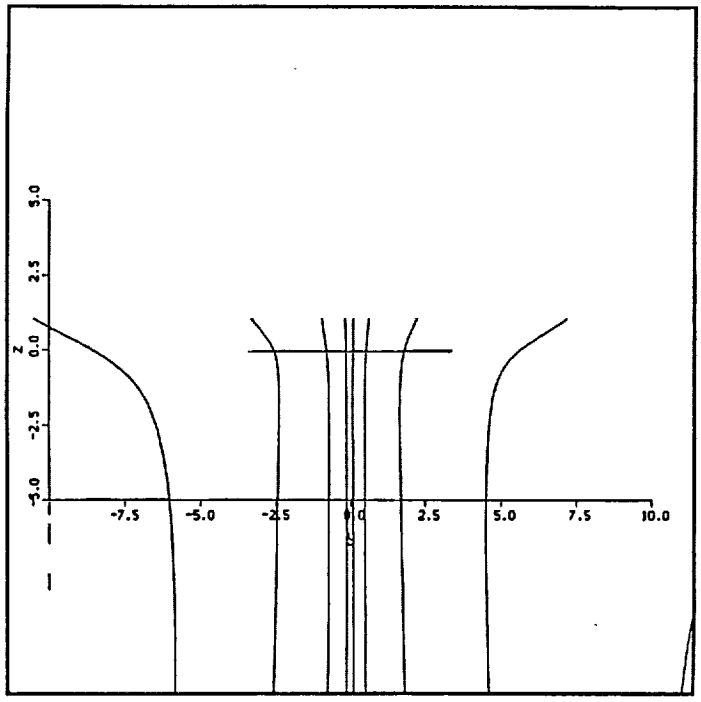

Figure 5.15: Particle traces in a vertical plane through the 3-D actuator disk, where $\Delta p = 0.05 p_\infty$.

Mach number contours in a vertical plane through the center of the actuator disk. Note that the flow accelerates smoothly through the disk and the flow gradients increase in the vicinity of the rotor, as expected. With the given pressure rise of 5% of freestream ambient pressure, a simple analysis assuming incompressible, 1-D flow and applying the Bernoulli equation above and below the rotor yields a maximum induced Mach number of 0.267. This quick check provides confidence in the CFD

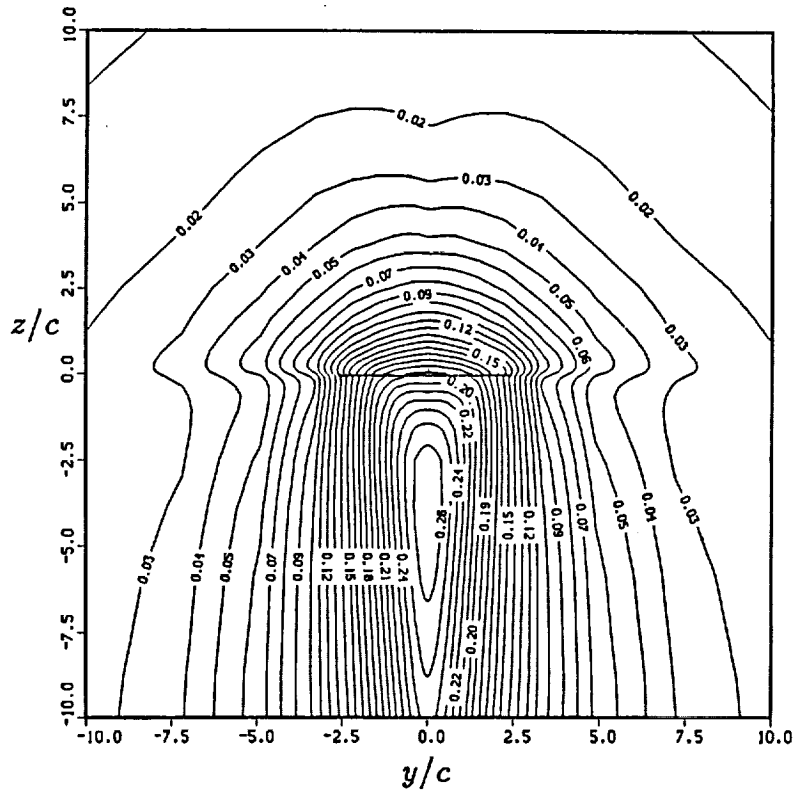

Figure 5.16: Mach number contours in a vertical plane through the 3-D actuator disk, where $\Delta p = 0.05 p_\infty$.

solution. As observed in the 2-D case, here also the rotor wake diffuses due to numerical dissipation.

Figure 5.17 shows the computed Mach contours in the plane of the rotor. The squared contours in the outer regions are due to a combination of insufficient grid point density and the contour plotting algorithm itself. Certainly, to study a rotor alone, a cylindrical mesh is more appropriate. A rectangular type of mesh, however, fits more easily in with the rest of the tilt rotor configuration.

Figures 5.18 and 5.19 show the effect of swirl on the flowfield. The tangential velocity (swirl) induced by the rotor is estimated from either experimental data or the momentum theory/blade element analysis discussed in Section 4.3 . For this test case, an arbitrary swirl Mach number of $M = 0.05$ is imposed uniformly on the upper boundary of the lower zone at the rotor location. The resulting flow pattern immediately downstream of the rotor is shown in Figure 5.18. It can be seen that the

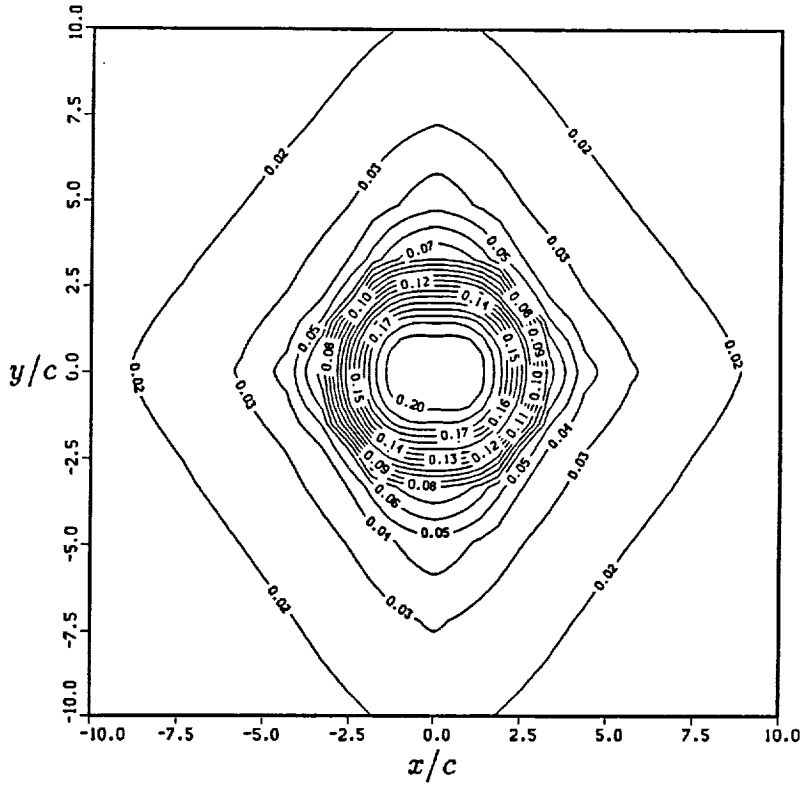

Figure 5.17: Mach number contours in the rotor plane, where $\Delta p = 0.05 p_\infty$.

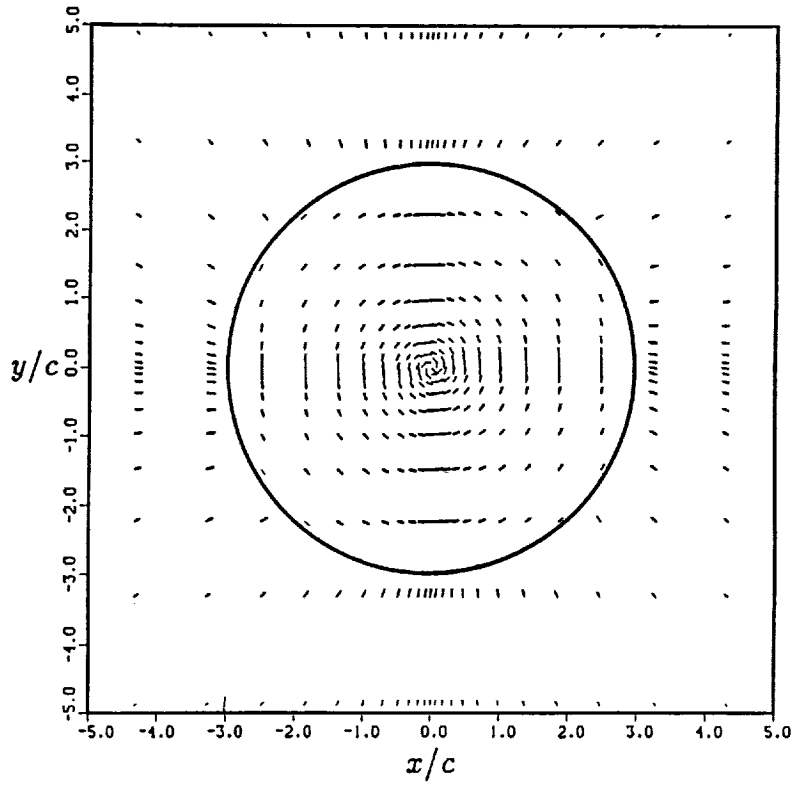

Figure 5.18: Velocity vectors in a horizontal plane immediately downstream of the rotor plane showing the effect of swirl, where $\Delta p = 0.05 p_\infty$ and $M_{swirl} = 0.05$.

flow beyond the rotor is influenced by the specified rotational motion. It is obvious from this plot that a greater number of grid points is required to better represent the physical extent of the rotor disk. Figure 5.19 is a projection of the particle traces onto a vertical plane running through the center of the rotor and wake. Clearly, the effect of the swirl imposed at the rotor face is communicated to the rotor wake.

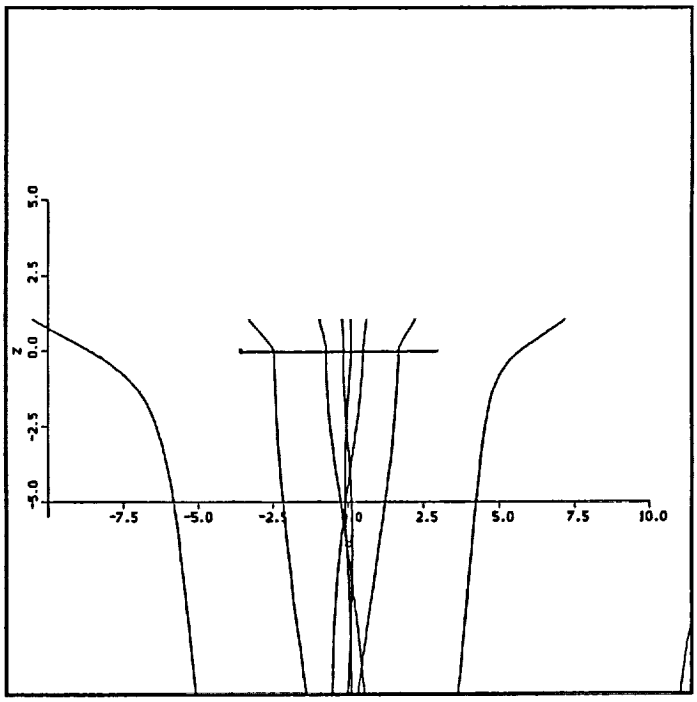

Figure 5.19: Particle traces projected on a vertical plane through the actuator disk showing the effect of swirl, where $\Delta p = 0.05 p_\infty$ and $M_{swirl} = 0.05$.

5.4 Wing/Rotor Interaction

5.4.1 Results in Two Dimensions

With the experience gained from studying the wing and airfoil in a freestream, and the rotor alone modeled using two zones, the computation of 2-D airfoil/rotor interaction is pursued. A more complicated grid is required. An inner zone is generated which extends from the airfoil surface to a flat boundary sufficiently wide to accommodate the complete rotor. Encircling this inner zone is another O-grid whose

inner boundary matches identically the outer boundary of the inner zone. The outer boundary of the outer grid extends about 20 rotor diameters in all directions – see Figures 5.20 and 5.21. The common boundary between the two zones is high-

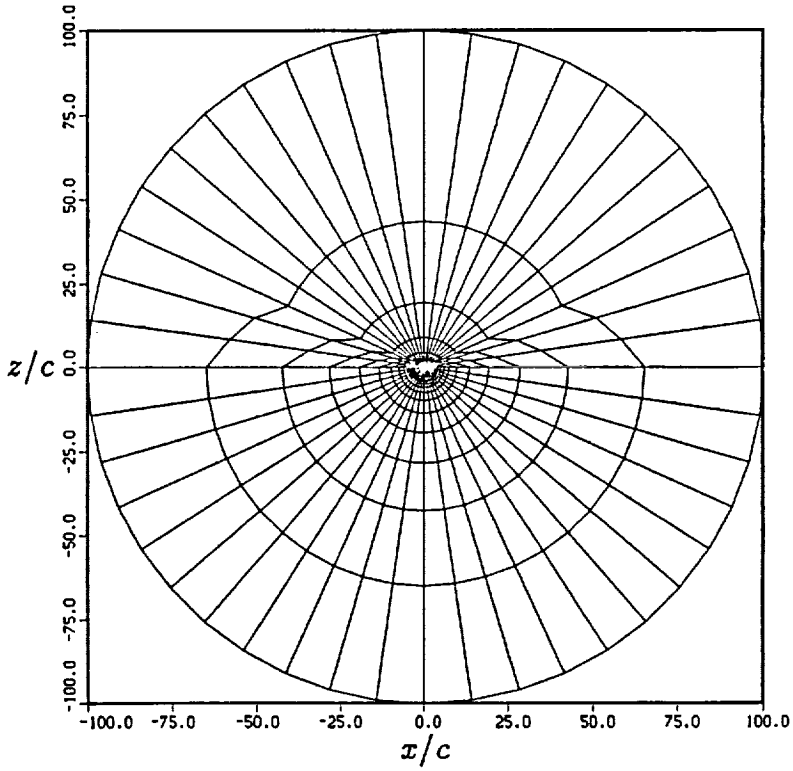

Figure 5.20: Farfield view of the 2-D, two-zone grid used for computations of wing/rotor interaction.

lighted. As in the freestream computations, 47 points are used to define the airfoil surface. In the inner zone, 22 points define each grid line normal to the surface. In the outer zone, 12 points define each grid line. Again, for "pseudo 2-D" calculations, five identical, parallel grid planes are required for the computation. The current grid is produced algebraically, resulting in some undesirable kinks in the grid interior. Smoother grids, using the elliptic grid solver, await future grid refinement.

Figures 5.22 and 5.23 show farfield and nearfield views, respectively, of the computed flowfield. The rotor diameter is 4.78 airfoil chords (determined from 0.16 scale model dimensions), and the uniform pressure rise across the rotor is $\Delta p = 0.05 p_\infty$. The rotor diameter and the rotor height above the airfoil, when non-dimensionalized

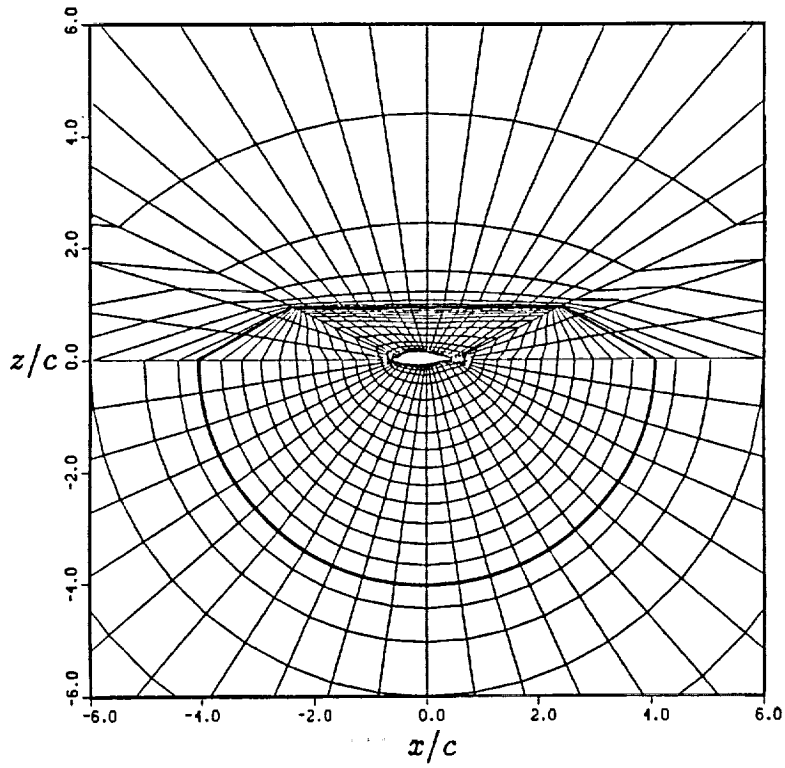

Figure 5.21: Nearfield view of the 2-D, two-zone grid used for computations of wing/rotor interaction.

by airfoil chord, all match the small scale model geometry of the past and projected future tests at NASA Ames Outdoor Aerodynamic Research Facility (OARF). For this hover calculation, M_∞ was set to 0.001 . The flow is driven purely by the $0.05p_\infty$ that is imposed across the zonal boundary at all points that lie within the rotor disk. Note that the near-stationary flow far above the rotor is pulled down into the rotor disk. The flow impinges on the airfoil where it stagnates at the mid-chord, bifurcates, and accelerates around the leading and trailing edges. An asymmetric separated flow region is produced beneath the airfoil very similar to that seen in the freestream calculations (refer to Figure 5.2). Again, as before, the Reynolds number is 0.5 x 10^6 and although turbulent flow is expected, only laminar calculations have been performed.

A moderately-loaded tilt rotor in hover produces an average pressure rise of around $0.01p_\infty$ across the rotor disk. Although good computational results have

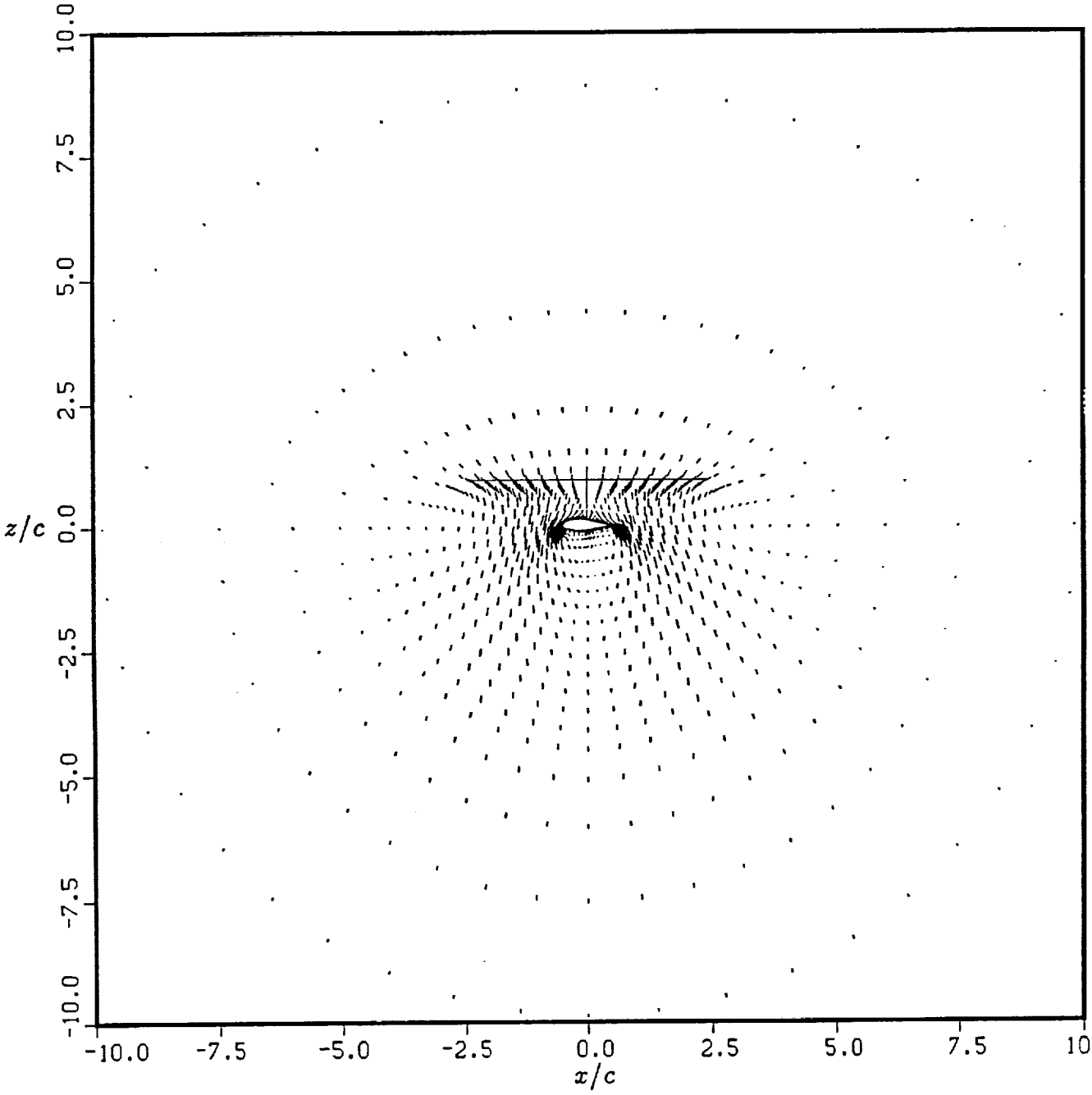

Figure 5.22: Farfield view of the velocity vectors for 2-D wing/rotor interaction, where $\Delta p = 0.05 p_\infty$ and the rotor diameter is 4.78.

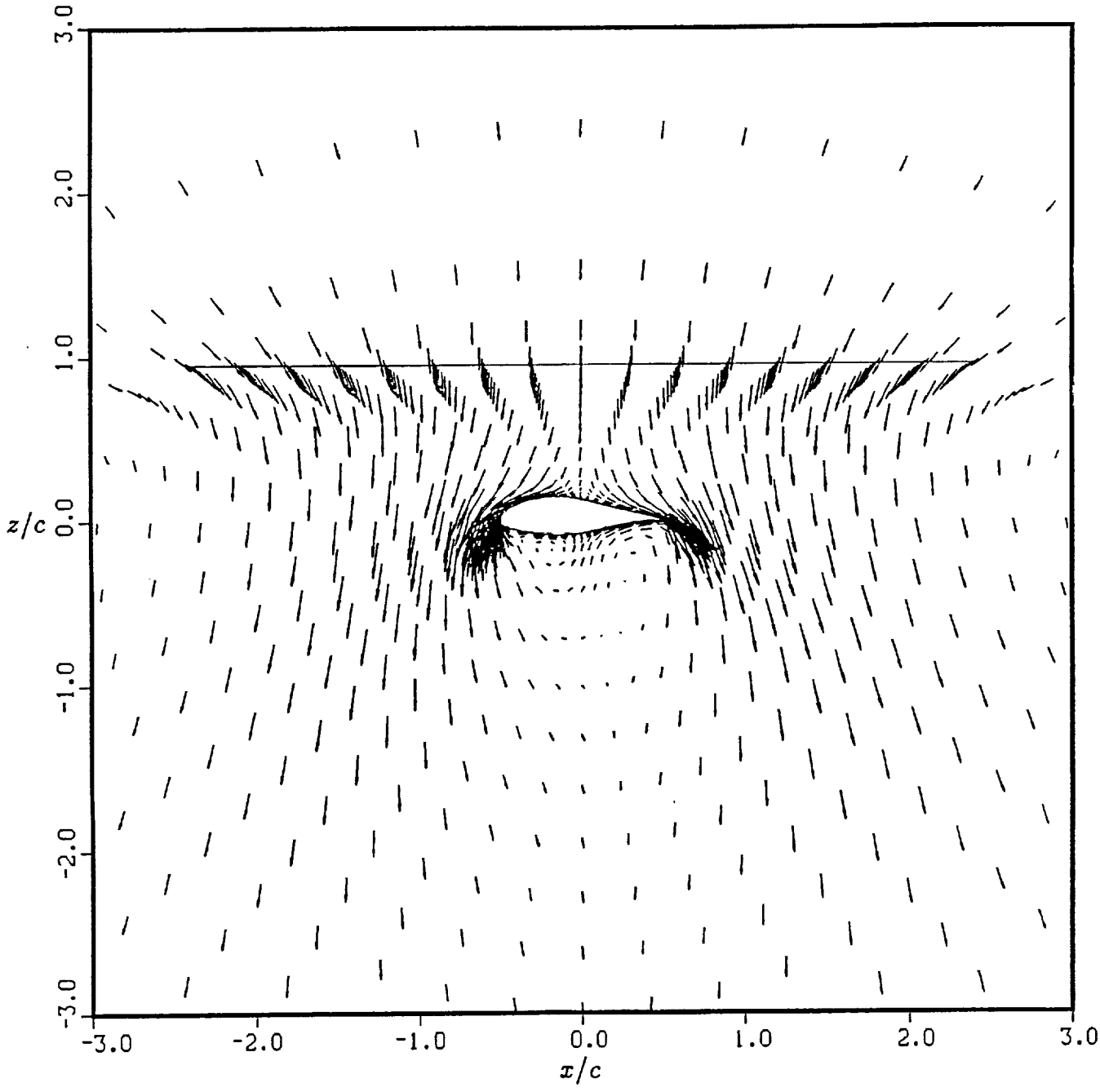

Figure 5.23: Nearfield view of the velocity vectors for 2-D wing/rotor interaction, where $\Delta p = 0.05 p_\infty$ and the rotor diameter is 4.78.

been obtained with this magnitude of pressure rise (refer to subsequent discussions), a higher Δp induces a higher Mach number flow which results in better solution convergence behavior for the compressible flow code. For program development purposes, then, a somewhat higher Δp is often used.

Figure 5.24 is a plot of the Mach number contours around the rotor and airfoil. The slight discontinuity in Mach contours through the rotor disk may be due to

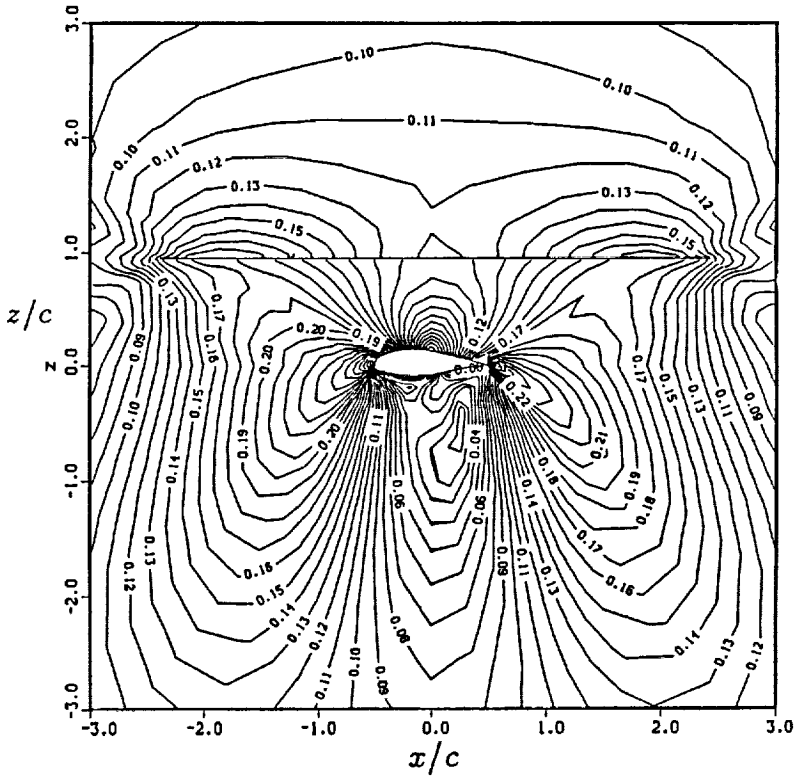

Figure 5.24: Mach number contours for 2-D wing/rotor interaction, where $\Delta p = 0.05 p_\infty$ and the rotor diameter is 4.78.

an insufficiently converged solution, or insufficient grid point density in this region. Figure 5.25 clearly shows the drop in static pressure as the rotor is approached from above and the pressure jump across the rotor. The influence of the wing on the pressure distribution at the rotor is made more obvious by comparing this plot with Figure 5.13 for a rotor alone (where the pressure is uniform along the width of the disk).

Figure 5.26 shows the static pressure distribution on the surface of the airfoil in

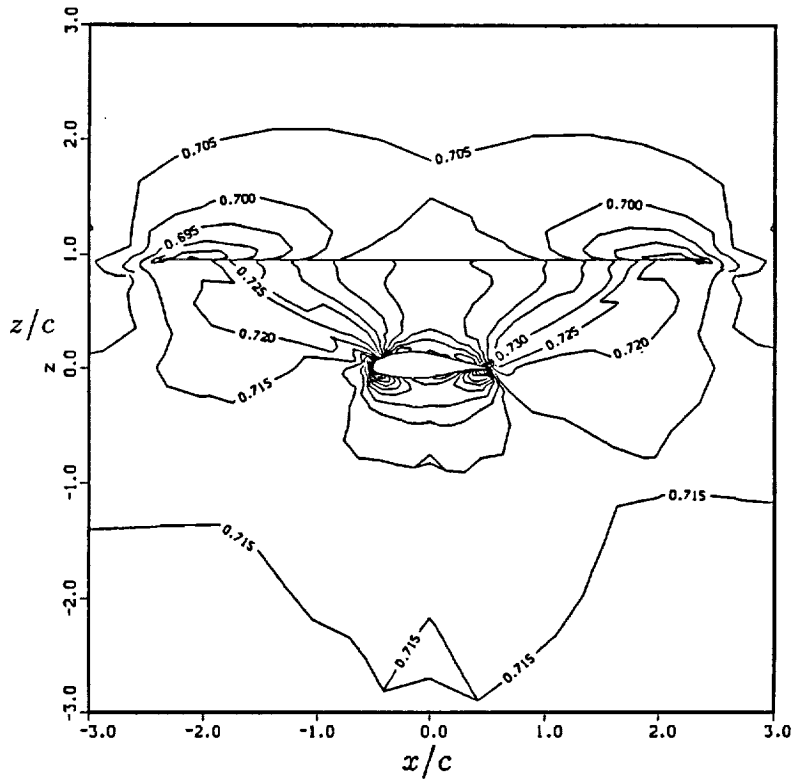

Figure 5.25: Pressure contours for 2-D wing/rotor interaction, where $\Delta p = 0.05 p_\infty$ and the rotor diameter is 4.78.

the presence of the lifting rotor. Note that for the non-dimensionalization used in the flow solver, $p_\infty = 1/\gamma = 0.7143$. The shape of the pressure distribution is very similar to that for an airfoil in $-90°$ freestream flow (Figure 5.5). These results are from steady-state (i.e. large time step) computations of the flow code. A time accurate calculation, on the other hand, yields a base pressure distribution that changes as a function of time (depending on the relative positions of the leading and trailing edge vortices with respect to the lower surface).

5.4.2 Results in Three Dimensions

A 2-zone grid suitable for computation of three-dimensional wing/rotor interaction is generated by stacking many 2-D grids in parallel. Various views of the 3-D mesh are shown in Figures 5.27 to 5.30. Figure 5.27 is a farfield view of the grid showing the outer dimensions. Figure 5.28 shows more details including the wing surface, and the inner and outer zones at the wing centerline ($y = 0$). The actual location of

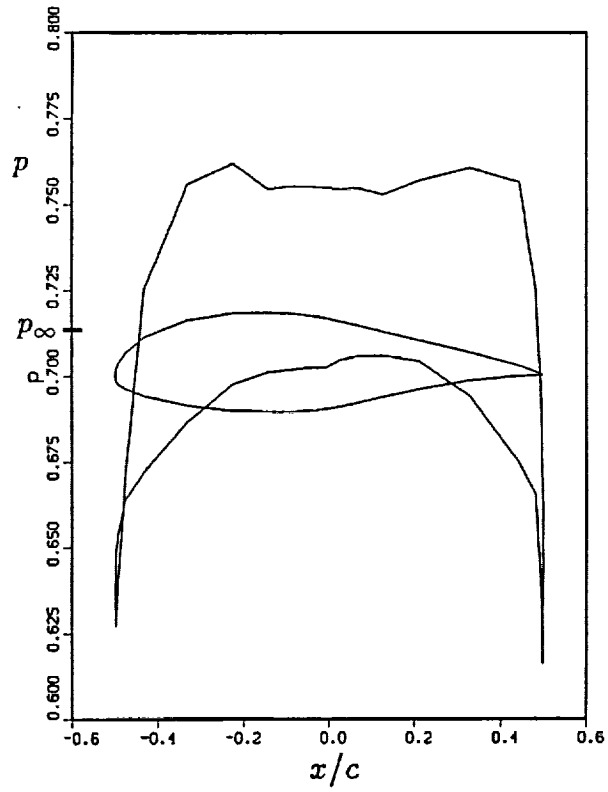

Figure 5.26: Pressure distribution on the surface of the airfoil for 2-D wing/rotor interaction, where $\Delta p = 0.05 p_\infty$ and the rotor diameter is 4.78.

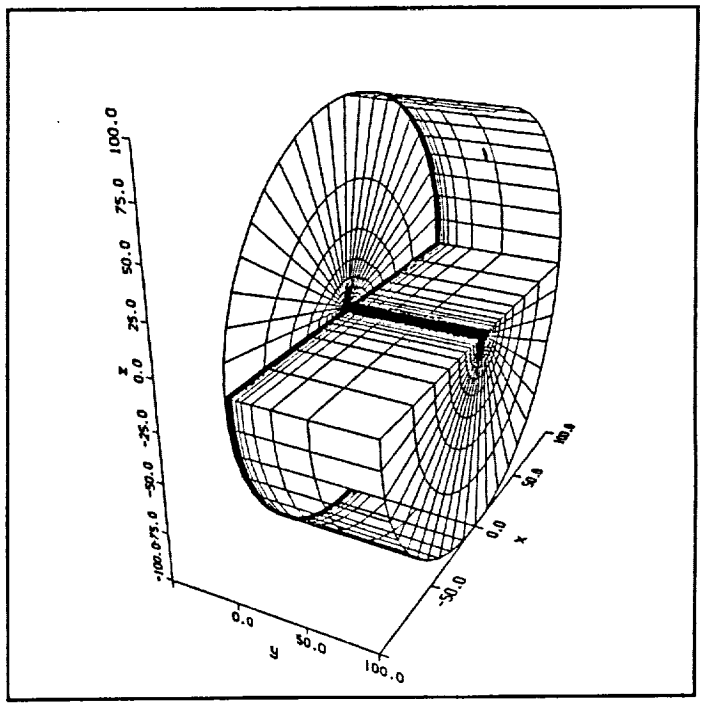

Figure 5.27: Farfield, cutaway view of the 3-D, two-zone grid used for computations of wing/rotor interaction.

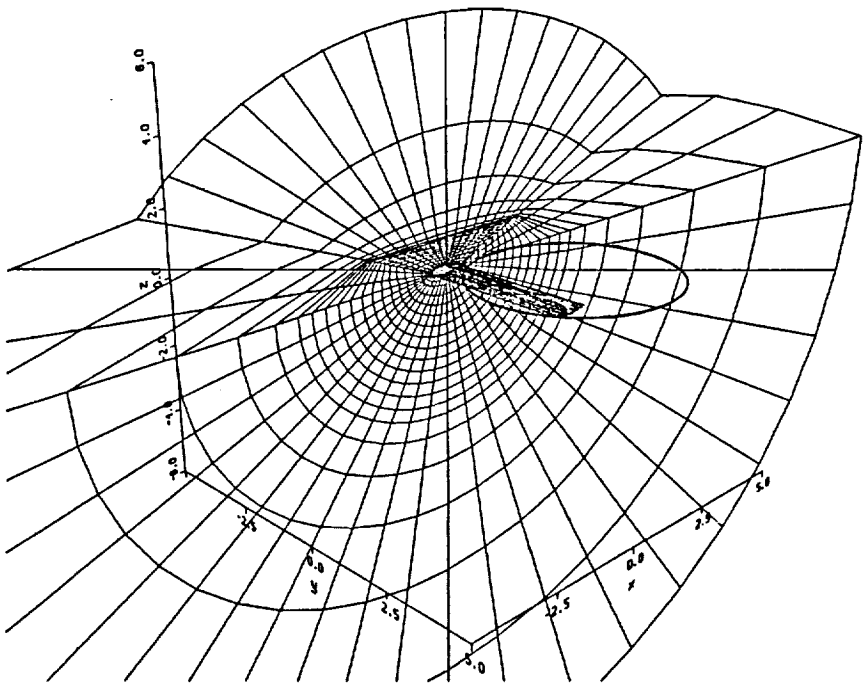

Figure 5.28: Nearfield, cutaway view of the 3-D, two-zone grid used for computations of wing/rotor interaction.

the rotor is superimposed on this view. Figure 5.29 is a horizontal cut in the plane of the rotor. The physical extent of the rotor disk is outlined here as well. Rotor boundary conditions are imposed at all points which lie on this plane and are within the rotor diameter. It is obvious from this figure that for accurate quantitative results, further grid refinement is required to define the rotor, particularly in the region outboard of the wing tip. Also, if the fountain effect is to be predicted, grid density must be increased in the centerline region of the mesh. The results presented here, therefore, are preliminary and are primarily qualitative in nature. Beyond the wing tip, those inner grid points which define the airfoil section, coalesce to essentially a single location as shown in Figure 5.30. This line which extends from the wing tip to the outer boundary in the spanwise direction is termed the "singular line". Boundary conditions must be imposed at all the coalesced points located on the singular line. All points immediately surrounding the singular line are used to

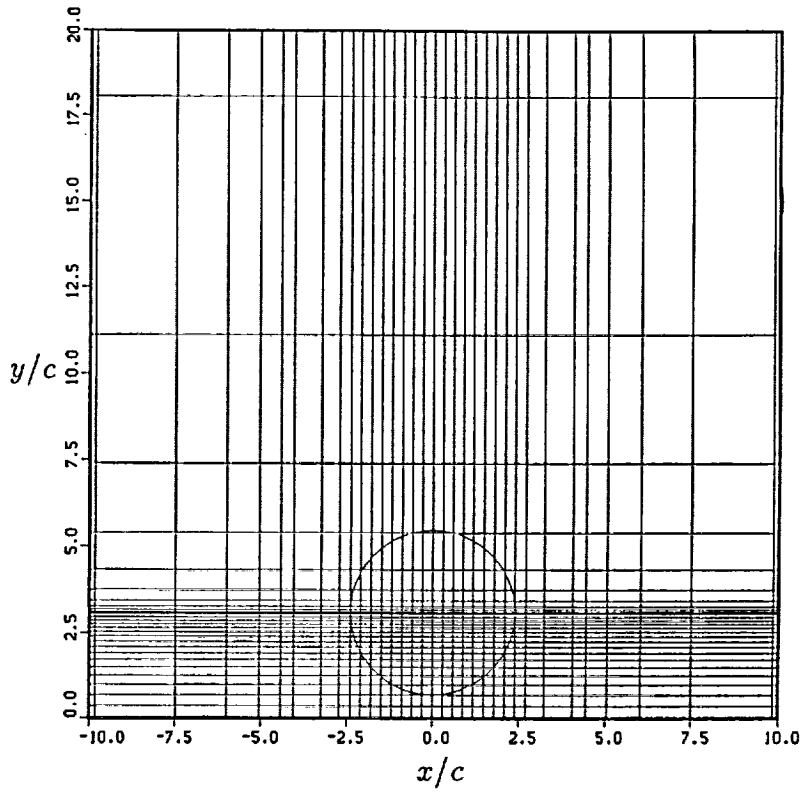

Figure 5.29: View in the plane of the rotor of the 3-D, two-zone grid used for computations of wing/rotor interaction.

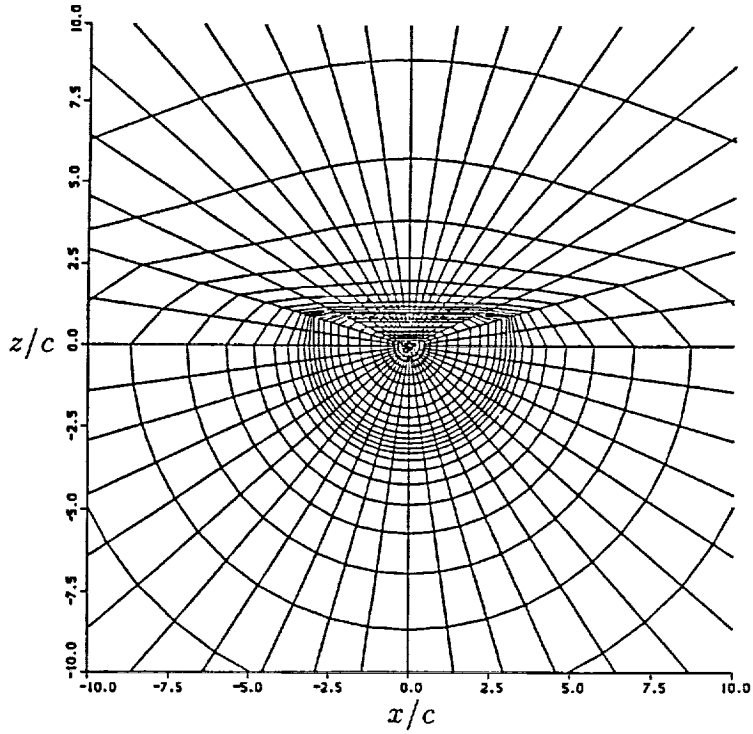

Figure 5.30: View of a vertical $x - z$ plane of the grid outboard of the wing tip of the 3-D, two-zone grid used for computations of wing/rotor interaction.

determine the average value of each of the flow properties. This is used to specify the boundary conditions on the singular line. This region, which is of no major concern in the freestream flow solutions, is seen to cause problems in the wing/rotor interaction calculations. This will be discussed in greater detail later.

For these calculations, a uniform Δp is again imposed across the rotor, but, for this case, a more representative value of $0.01p_\infty$ is used.

Figure 5.31 shows the Mach number contours in a vertical $x-z$ plane at the mid semi-span location. For this calculation, the Mach contours pass smoothly through

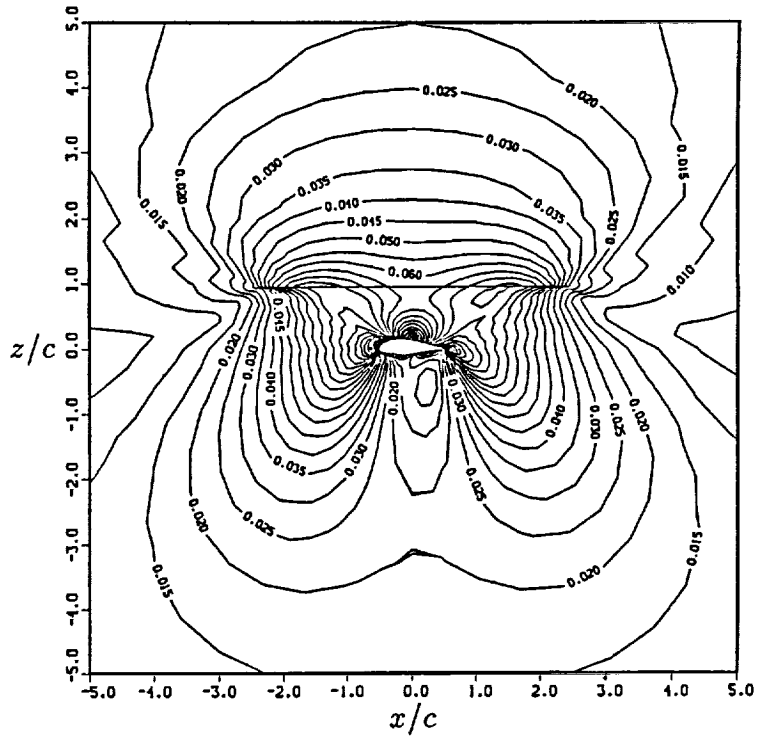

Figure 5.31: Mach number contours in a vertical plane through the mid semi-span location for 3-D wing/rotor interaction, where $\Delta p = 0.01p_\infty$ and the rotor diameter is 4.78.

the rotor. Figure 5.32 is the corresponding plot for the static pressure contours.

Figures 5.33 to 5.35 are all views of flow properties in a vertical plane that runs spanwise through the wing mid-chord. The rotor location is superimposed on these plots. Intuitively, the flow above the wing seems to have been computed correctly. The flow stagnates in the mid-chord region at the semi-span location corresponding

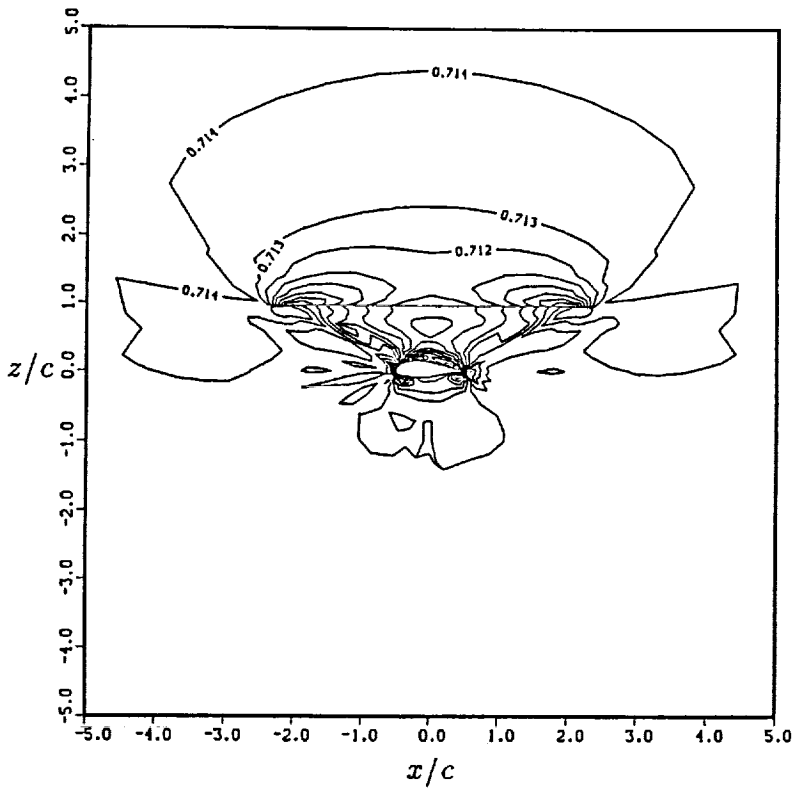

Figure 5.32: Pressure contours in a vertical plane through the mid semi-span location for 3-D wing/rotor interaction, where $\Delta p = 0.01 p_\infty$ and the rotor diameter is 4.78.

to about $y/c = 2.0$. From this point the flow is divided into two opposite spanwise directions – towards the tip and towards the wing root.

Beyond the wing tip, however, the singular line of the grid is affecting the results. It seems to be acting as a source, producing a discontinuity in velocity along its length. The reason for this behavior is as yet unknown. Figure 5.36 is a view of the Mach number contours in a vertical $x - z$ plane beyond the wing tip. A large gradient in flow velocity is produced in a very localized region. The singular line boundary conditions are treated identically for the 3-D freestream computations, and, as previously mentioned, no anomaly was found for that case (see Section 5.2.2). It is possible that there may be some inconsistency in the application of the boundary conditions for the rotor, and that this may be affecting the computation on the inner boundary that contains the singular line. Various attempts at correcting the situation have so far been unsuccessful. One way to eliminate the problem is to develop a grid

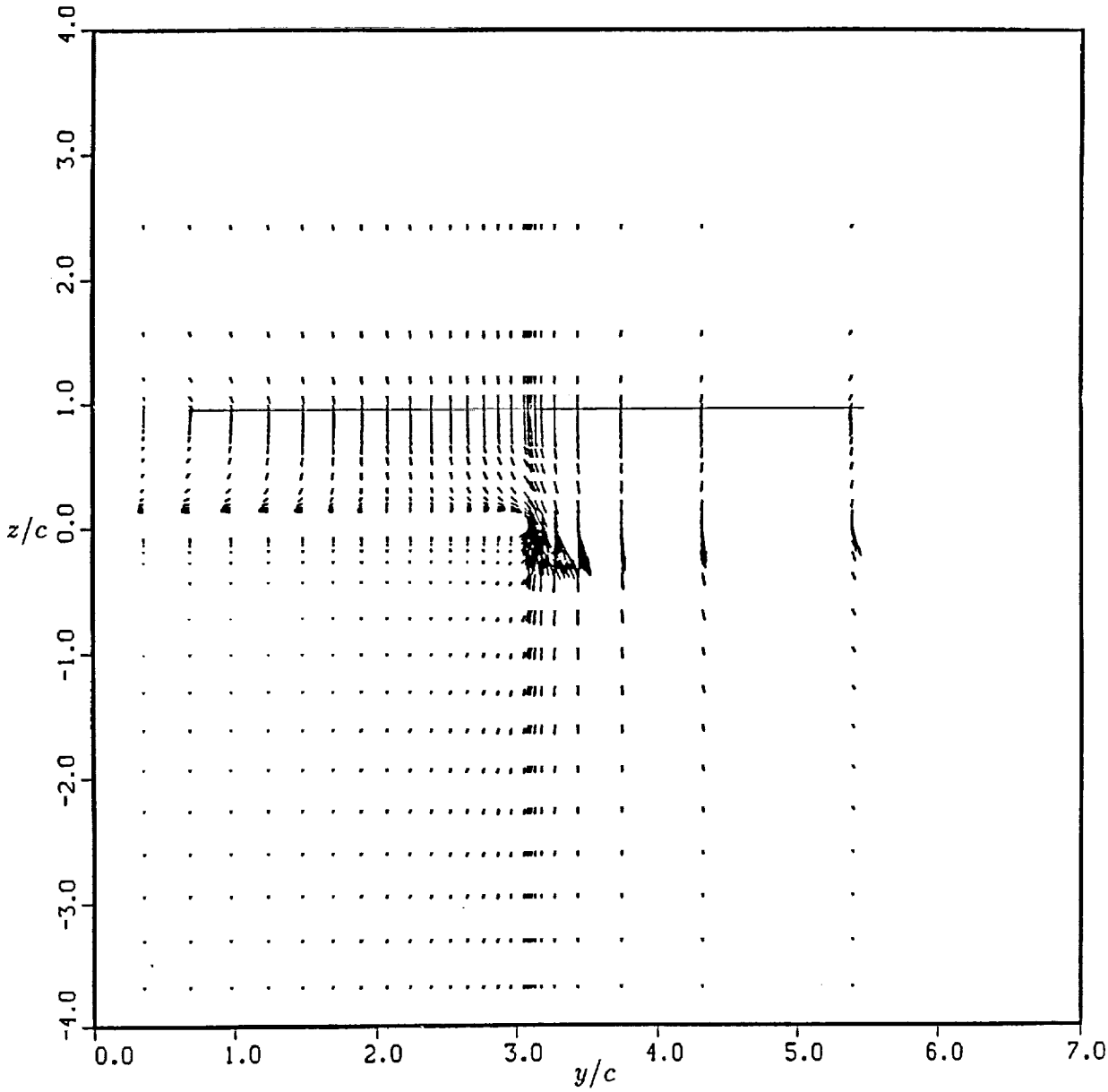

Figure 5.33: Velocity vectors in a vertical, spanwise plane through the wing mid-chord for 3-D wing/rotor interaction, where $\Delta p = 0.01 p_\infty$ and the rotor diameter is 4.78.

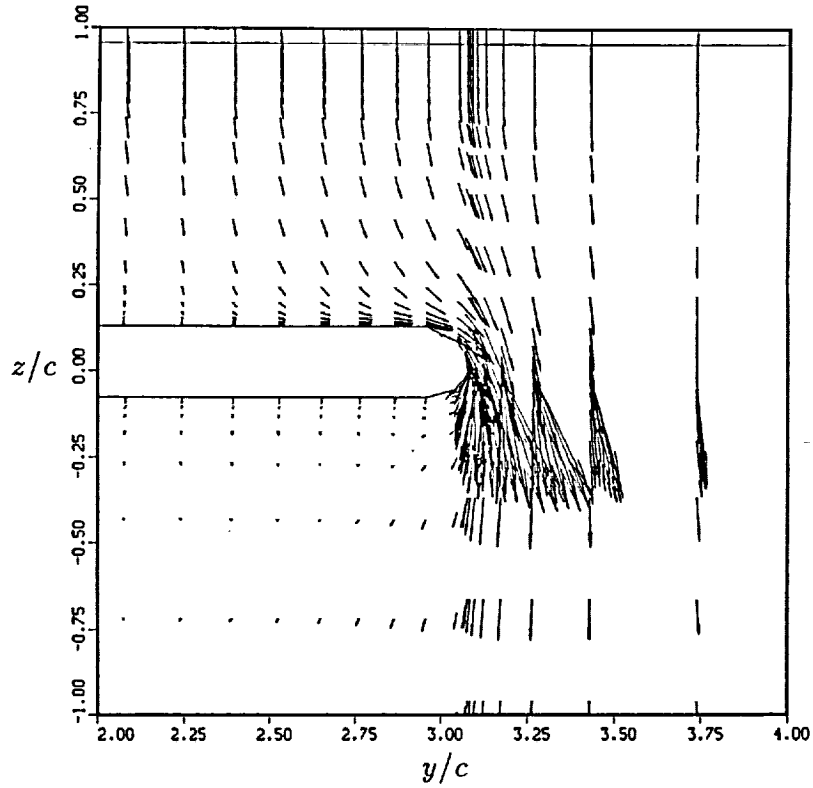

Figure 5.34: Velocity vectors around the wing tip in a vertical, spanwise plane through the wing mid-chord for 3-D wing/rotor interaction, where $\Delta p = 0.01 p_\infty$ and the rotor diameter is 4.78.

with no singular line. Although grid generation becomes considerably more complex, this approach is currently being pursued.

5.5 Wall Jet in Two Dimensions

Some preliminary results for tangential blowing near the leading edge have also been obtained. The furthest forward slot on the 0.18 scale model soon to be tested at NASA Ames' OARF is located at 8.1% of the airfoil chord from the leading edge. A tangential jet at this location is modeled by imposing a jet velocity at the appropriate grid locations. This jet velocity is derived by assuming isentropic expansion from the plenum within the airfoil where the total pressure is specified. Assuming a plenum pressure 8% above freestream ambient pressure, the jet velocity at the plenum exit is about $M = 0.3$. Figure 5.37 is a plot of the velocity vectors for a 2-D wing/rotor interaction case with tangential leading edge blowing. A uniform pressure rise of

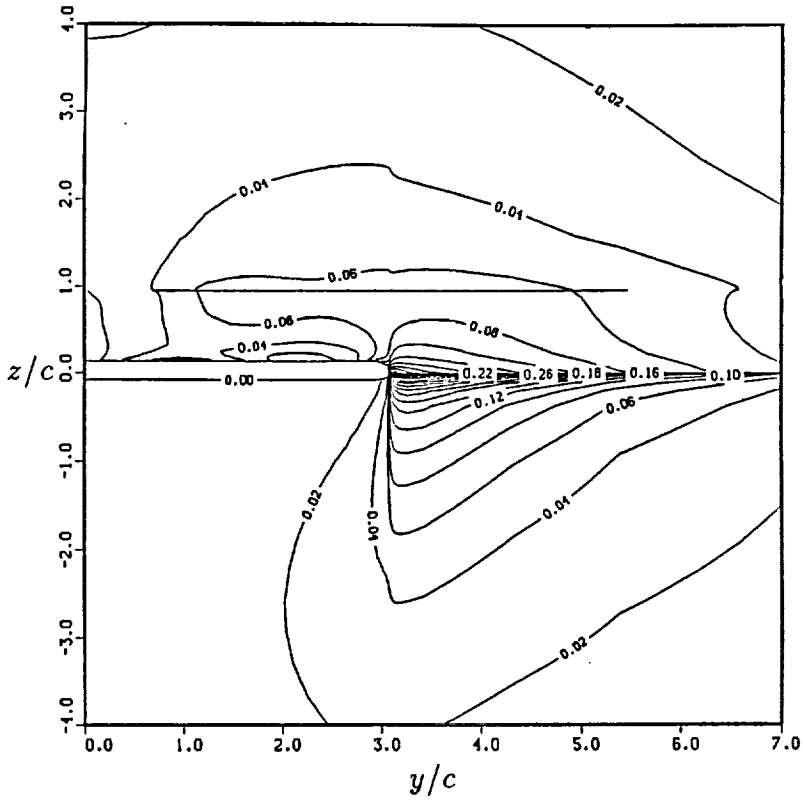

Figure 5.35: Mach number contours in a vertical, spanwise plane through the wing mid-chord for 3-D wing/rotor interaction, where $\Delta p = 0.01 p_\infty$ and the rotor diameter is 4.78.

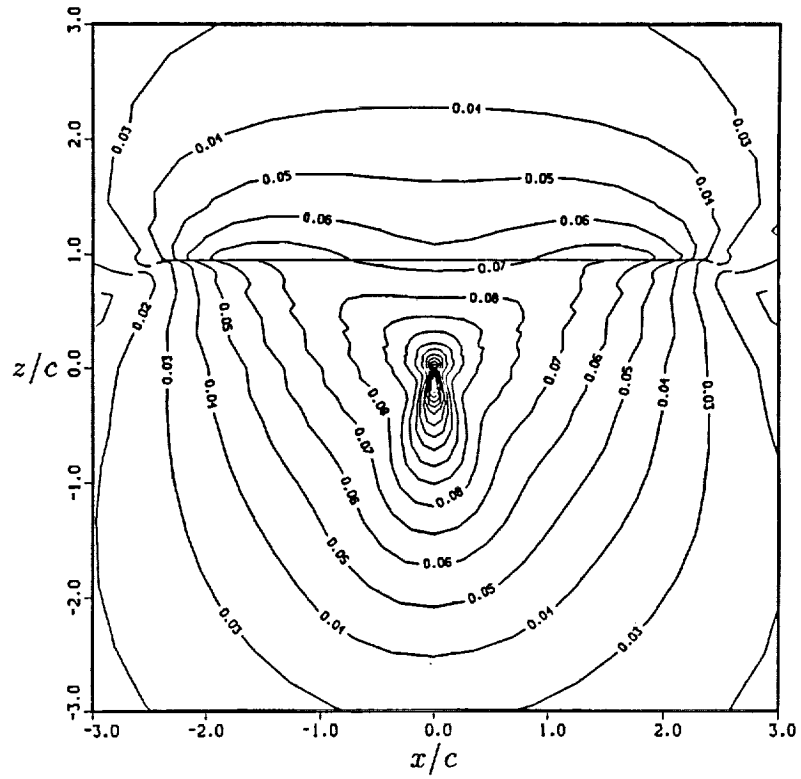

Figure 5.36: Mach number contours in a vertical $x - z$ plane beyond the wing tip for 3-D wing/rotor interaction, where $\Delta p = 0.01 p_\infty$ and the rotor diameter is 4.78.

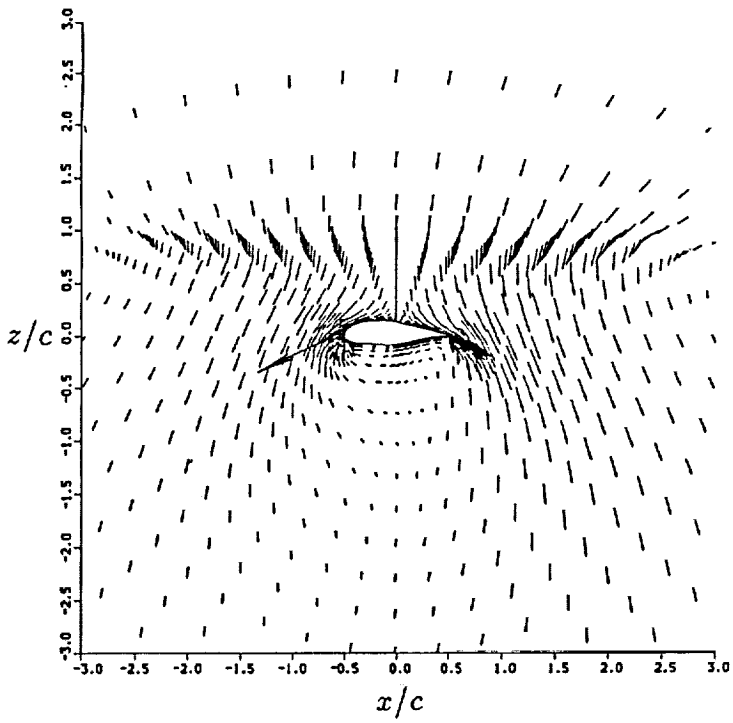

Figure 5.37: Velocity vectors for a 2-D wing/rotor interaction case with tangential wall blowing, where the plenum pressure is $1.08p_\infty$, $\Delta p = 0.05p_\infty$ across the rotor, and $M_\infty = 0.001$.

$0.05p_\infty$ across the rotor is specified for this hover calculation. It can be seen that the magnitude of the jet velocity far exceeds any of the rotor-induced flow velocities.

Figure 5.38 is a close-up view of the jet velocity profiles in the downstream of the jet exit. This case assumes a freestream flow of $M_\infty = 0.2$ at $-90°$, in addition to a rotor pressure rise of $0.03p_\infty$. The plenum pressure, as before, is $1.08p_\infty$. Of interest in this plot is the evolution of the velocity profiles as the outer flow is entrained by the jet through momentum transfer due to viscous effects within the boundary layer.

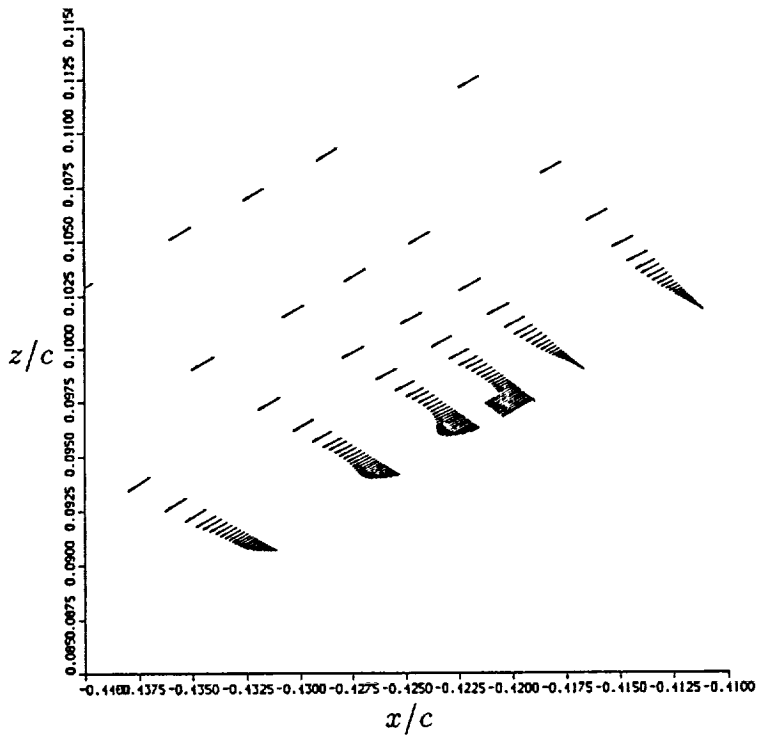

Figure 5.38: Close-up view of velocity vectors for a 2-D wing/rotor interaction case with tangential wall blowing, where the plenum pressure is $1.08p_\infty$, $\Delta p = 0.03p_\infty$ across the rotor, and $M_\infty = 0.2$.

Chapter 6

Conclusions and Recommendations

6.1 Conclusions

The research undertaken to date has demonstrated the feasibility of analyzing the tilt rotor flowfield using the thin-layer Navier-Stokes equations and an implicit, finite difference technique to solve them. Computational fluid dynamics promises to yield the most accurate, theoretical prediction of download yet. Good results have been obtained for the V-22 airfoil and wing in a low subsonic Mach number flow (M_∞ = 0.2) at -90 degrees. The use of multiple grid zones has enabled a more accurate representation of the full rotor flowfield. A rotor alone in two and three dimensions has been modeled using two zones. The results are very good and can be further improved by grid refinement. Wing/rotor interaction has been modeled in such a way that rotor and wing flows are partially coupled. Although the Δp across the rotor remains fixed, the pressures in the rotor plane are influenced by the wing which lies less than a chord length below the rotor. Good results in two dimensions have been obtained for a lifting rotor in hover. In three dimensions, the flow computed over the wing looks intuitively correct, but beyond the wing tip, the presence of the singular line in the grid causes a local discontinuity in the computed flowfield. This problem is currently being investigated. Finally, preliminary results obtained for tangential

leading edge blowing in two dimensions look very encouraging.

6.2 Recommendations

6.2.1 Near Term

It is first desired to improve the three-dimensional wing/rotor interaction solution by solving the problem associated with the singular line in the grid outboard of the wing tip. Perhaps an inconsistency in the boundary conditions exists that could be alleviated by improved implementation. Alternatively, a new, albeit more complicated, grid could be generated which has no singular line.

The elliptic grid solver should be employed with the boundary control suggested by Sorrenson and Steger. This would smooth the interior grid point distributions and remove the kinks, thereby improving spatial accuracy of the solution.

Modification of the code to allow for non-uniform, radial distributions of pressure rise and swirl is a fairly straight-forward task.

A turbulence model should be implemented. A Baldwin-Lomax model would be adequate for the boundary layer, and Roberts' model would be suitable for the curved jet region.

Tangential leading edge blowing over the finite wing should also be implemented.

The above modifications should be followed by detailed flow calculations and comparisons with available experimental results obtained in scale model tilt rotor tests by the Rotorcraft Aeromechanics Branch of the Full Scale Aerodynamics Division of NASA Ames Research Center. Effect of rotor thrust coefficient, swirl velocity, swirl direction, jet blowing strength and location, on the wing download should be studied.

It is the intention of the authors to pursue these near term recommendations during the coming year.

6.2.2 Far Term

In the far term, there are several improvements to the methodology that could be introduced to yield a computation that is more accurate and more representative of an actual tilt rotor vehicle.

One of first areas of focus would be the rotor. Eventually, at some point in the future when computational resources become available, it would be desirable to perform a time-accurate Navier-Stokes calculation about each of the rotating blades of the rotor and to couple that with the solution of the rest of the tilt rotor flowfield. In the interim, however, incorporating the momentum theory/blade element analysis into the Navier-Stokes flow solver would be a considerable improvement. This would allow radial and azimuthal variations of flow properties on the rotor disk that would also be influenced by the wing. Δp, for example, would not be fixed prior to the Navier-Stokes calculation but would result from it. The improved rotor model could be incorporated into the boundary conditions of the flow solver at a common boundary between two zones. Alternatively, by adding momentum source terms to the momentum equations of the Navier-Stokes equations, the rotor could be defined at any desired set of grid points in the mesh interior, thus eliminating the need for a zonal approach to rotor modeling. It is recommended that both of the approaches be attempted, and the results compared.

Modeling the engine pylon and the fuselage are obvious improvements that would help yield a more accurate representation of the actual tilt rotor aircraft. This, of course, would entail complex grid generation. In the same vein, incorporation of a trailing edge flap in the airfoil grid would be helpful in the analysis of the effect of download due to flap deflection.

A greater degree of accuracy in the modeling of the separated flow region would be attained if the full Navier-Stokes equations are solved. Also, an improved turbulence model developed specifically for bluff body flows would definitely improve the results

even further. A computation which is second-order accurate in time might also be attempted to better resolve the unsteadiness of the flow.

Implementation of the above recommendations is a challenging task, but one that would be invaluable in the pursuit of the complete understanding of the complicated tilt rotor flowfield.

Bibliography

[1] Rosenstein, H. and Clark, R.,"Aerodynamic Development of the V-22 Tilt Rotor", AIAA Paper 86-2678, AIAA/AHS/ASEE Aircraft Systems, Design & Technology Meeting, Dayton, Ohio, 1986.

[2] Fort, F. F. and Light, J., "Rotor/Wing Aerodynamic Interactions in Hover", NASA TM 88255, 1986.

[3] McVeigh, M. A., "The V-22 Tilt-Rotor Large-Scale Rotor Performance/Wing Download Test and Comparison with Theory", Vertica, Vol. 10, No. 3/4, 1986.

[4] Maisel, M. and Harris, D., "Hover Tests of the XV-15 Tilt Rotor Research Aircraft", AIAA Paper 81-2501, AIAA/SETP/SFTE/SAE/ITEA/IEEE 1st Flight Test Conf., Las Vegas, 1981.

[5] McCroskey, W., Spalart, P., Laub, G., Maisel, M., and Maskew, B., "Airloads on Bluff Bodies, with Application to the Rotor-Induced Downloads on Tilt-Rotor Aircraft", Vertica, Vol.9, No.1, 1985.

[6] Maisel, M., Laub, G., and McCroskey, W. , "Aerodynamic Characteristics of Two-Dimensional Wing Configurations at Angles of Attack Near $-90°$", NASA TM 88373, 1986.

[7] McVeigh, M., Grauer,W., and Paisley, D., "Rotor/Airframe Interactions on Tiltrotor Aircraft", Proceedings of the 44th Annual Forum of the American Helicopter Society, Washington, D.C., June 1988.

[8] Clark, D., "Analysis of the Wing/Rotor and Rotor/Rotor Interactions Present in Tilt-Rotor Aircraft", Vertica, Vol.11, No.4, 1987.

[9] Clark, D. and McVeigh, M., "Analysis of the Wake Dynamics of a Typical Tilt-Rotor Configuration in Transition Flight", Paper No. 28, 11th European Rotorcraft Forum, London, England, 1985.

[10] Lee, C. S.,"A Two Dimensional Study of Rotor/Airfoil Interaction in Hover", JIAA TR-88, Stanford University, 1988.

[11] Srinivasan, G. and McCroskey, W., "Navier-Stokes Calculations of Hovering Rotor Flowfields", AIAA Paper 87-2629-CP, AIAA Atmospheric Flight Mechanics Conf., Monterey, California, 1987.

[12] Srinivasan, G. and McCroskey, W.,"Numerical Simulations of Unsteady Airfoil-Vortex Interactions", Vertica, Vol.11, No.1/2, 1987.

[13] Roberts, T. W., "Euler Equation Computations for the Flow Over a Hovering Helicopter Rotor", NASA CR 177493, 1988.

[14] McCroskey, W. and Baeder, J., "Some Recent Advances in Computational Aerodynamics for Helicopter Applications", NASA TM 86777, 1985.

[15] Rajagopalan, R. G. and Mathur, S. R., "Three Dimensional Analysis of a Rotor in Forward Flight", AIAA Paper 89-1815, AIAA 20th Fluid Dynamics, Plasma Dynamics and Lasers Conf., Buffalo, 1989.

[16] Fujii, K. and Obayashi, S., "Practical Applications of New LU-ADI Scheme for the Three-Dimensional Navier-Stokes Computation of Transonic Viscous Flows", AIAA Paper 86-0513, AIAA 24th Aerospace Sciences Meeting, Reno, 1986.

[17] Fujii, K. and Obayashi, S., "Navier-Stokes Simulation of Transonic Flow over Wing-Fuselage Combinations", AIAA Paper 86-1831, AIAA 4th Applied Aerodynamics Conf., San Diego, 1986.

[18] Obayashi, S. and Kuwahara, K., "An Approximate LU Factorization Method for the Compressible Navier-Stokes Equations", Journal of Computational Physics, Vol.63, 1986.

[19] Yeh, D.,"Numerical Study of Delta Wing Leading Edge Blowing", JIAA TR-86, Stanford University, 1988.

[20] Viviand, H., "Formes Conservatives des Équations de la Dynamique des Gaz", LaRecherche Aérospatiale, No.1, 1974.

[21] Vinokur, M., "Conservation Equations of Gasdynamics in Curvilinear Coordinate Systems", Journal of Computational Physics, No.14, 1974.

[22] Baldwin, B. and Lomax, H., "Thin Layer Approximation and Algebraic Model for Separated Turbulent Flows", AIAA Paper 78-257, AIAA 16th Aerospace Sciences Meeting, Huntsville, Alabama, 1978.

[23] Roberts, L., "A Theory for Turbulent Curved Wall Jets", AIAA Paper 87-0004, AIAA 25th Aerospace Sciences Meeting, Reno, 1987.

[24] Beam, R. M. and Warming, R. F., "An Implicit Finite-Difference Algorithm for Hyperbolic Systems in Conservation-Law Form", Journal of Computational Physics, Vol.22, 1976.

[25] Pulliam, T. and Steger, J.,"Implicit Finite-Difference Simulations of Three-Dimensional Compressible Flow", AIAA Journal, Vol.18, No.2, 1980.

[26] Pulliam, T., "Euler and Thin Layer Navier-Stokes Codes: ARC2D, ARC3D", Notes for Computational Fluid Dynamics User's Workshop, The University of

Tennessee Space Institute, Tullahoma, Tennessee, March 12-16, 1984.

[27] Pulliam, T. and Chaussee, D., "A Diagonal Form of an Implicit Approximate-Factorization Algorithm", Journal of Computational Physics, Vol.39, 1981.

[28] Steger, J. and Warming, R., "Flux Vector Splitting of the Inviscid Gasdynamic Equations with Application to Finite-Difference Methods", Journal of Computational Physics, Vol.40, 1981.

[29] Lombard, C., Bardina, J., Venkatapathy, E., and Oliger, J., "Multi-Dimensional Formulation of CSCM - An Upwind Flux Difference Eigenvector Split Method for the Compressible Navier-Stokes Equations", AIAA Paper 83-1895, AIAA 6th CFD Conf., Danvers, Massachusetts, 1983.

[30] Guruswamy, G. P., "Time-Accurate Unsteady Aerodynamic and Aeroelastic Calculations of Wings Using Euler Equations", AIAA Paper 88-2281, AIAA/ASME/ASCE/AHS 29th Structures, Structural Dynamics and Materials Conf., Williamsburg, Virginia, 1988.

[31] Guruswamy, G. P., "Numerical Simulation of Vortical Flows on Flexible Wings", AIAA Paper 89-0537, AIAA 27th Aerospace Sciences Meeting, Reno, 1989.

[32] Pulliam, T. and Steger, J., "Recent Improvements in Efficiency, Accuracy, and Convergence for Implicit Approximate Factorization Algorithms", AIAA Paper 85-0360, AIAA 23rd Aerospace Sciences Meeting, Reno, 1985.

[33] Chaussee, D., Kutler, P., and Pulliam, T. , "Three Dimensional Viscous Flow Field Program. Part 1. Viscous Blunt Body Program (Interim Report)", AFWAL-TM-81-63-FIMG, Flight Dynamics Laboratory, Air Force Wright Aeronautical Laboratories, Wright-Patterson Air Force Base, Ohio, 1981.

[34] Steger, J., "Implicit Finite Difference Simulation of Flow About Arbitrary Geometries with Application to Airfoils", AIAA Paper 77-665, AIAA 10th Fluid & Plasmadynamics Conf., Albuquerque, New Mexico, 1977.

[35] Thompson, J., Thames, F., and Mastin, C., "Automatic Numerical Generation of Body-Fitted Curvilinear Coordinate System for Field Containing Any Number of Arbitrary Two-Dimensional Bodies", Journal of Computational Physics, Vol.15, 1974.

[36] Thompson, J., Thames, F., Mastin, C., and Shanks, S., "Use of Numerically Generated Body-Fitted Coordinate Systems for Solutions of the Navier-Stokes Equations", AIAA 2nd CFD Conf., Connecticut, 1975.

[37] Holst, T. L., "Numerical Computation of Transonic Flow Governed by the Full-Potential Equation", NASA TM 84310, 1983.

[38] Sorenson,R. and Steger, J., "Numerical Generation of Two-Dimensional Grids by the Use of Poisson Equations with Grid Control at the Boundaries", Proc. of the Numerical Grid Generation Techniques Workshop, Langley Research Center, NASA, Hampton, Va., NASA CP-2166, 1980.

[39] Glauert, H., The Elements of Airfoil and Airscrew Theory, Cambridge University Press, London, 1930.

[40] McCormick, B. W., Aerodynamics of V/STOL Flight, Academic Press, New York, 1967.

[41] Prouty, R. W., Helicopter Performance, Stability, and Control, PWS Publishers, Boston, 1986.

[42] Tavella, D., Private Communication.

[43] Buning, P. and Steger, J., "Graphics and Flow Visualization in Computational Fluid Dynamics", AIAA Paper 85- 1507, AIAA 7th CFD Conf., Cincinnati, 1985.

[44] Walatka, P. and Buning, P., " PLOT3D User's Manual", NASA TM 101067, 1989.

[45] Massey, B. S. , Mechanics of Fluids, 3rd Edition, Van Nostrand Reinhold Co., London, 1976.